

A Primer on Far-Infrared Polarimetry

R. H. HILDEBRAND,^{1,2} J. A. DAVIDSON,³ J. L. DOTSON,⁴ C. D. DOWELL,⁵ G. NOVAK,⁶ AND J. E. VAILLANCOURT¹

Received 2000 March 8; accepted 2000 April 27

ABSTRACT. We present an introduction to observing procedures and principles of analysis used in far-infrared polarimetry. The observing procedures are those for single-dish observations of thermal emission from aligned dust grains. We discuss techniques for removing backgrounds and for reducing and evaluating errors. The principles of analysis are those required for interpreting polarization maps and polarization spectra in terms of opacity, field structure, and variations in temperature and polarizing efficiency.

1. INTRODUCTION

The earliest detections of polarized emission from Galactic clouds at far-infrared and submillimeter wavelengths (Cudlip et al. 1982; Hildebrand, Dragovan, & Novak 1984; Dragovan 1986; Barvainis, Clemens, & Leach 1988; Flett & Murray 1991) were restricted to intensity peaks of bright molecular clouds. As the instruments and techniques improved (Platt et al. 1991; Schleuning et al. 1997; Dowell et al. 1998; Holland et al. 1999), it became evident that thermal emission from interstellar dust is measurably polarized at almost every point in every cloud (e.g., Hildebrand 1996; Dotson et al. 2000). The flux densities required for adequate signals dropped from more than 10,000 Jy beam⁻¹ in 1984 to ~ 1 Jy beam⁻¹ in 2000, the number of pixels increased from 1 to as many as 91, and the resolution improved from 2' to $\sim 10''$ (or less than 2'' for bright objects with current interferometry). One can expect continuing gains in sensitivity, array size, and resolution.

The advances in instrumentation have made it possible to use polarimetry to trace magnetic fields not only in the cores and envelopes of bright molecular clouds but also in thermal streamers (Morris, Davidson, & Werner 1995; Davidson 1996), disks around T Tauri stars (Tamura et al. 1999), envelopes of young stellar objects (Vallée & Bastien 2000), and other sources of dust emission. Comparisons of

polarization maps at different wavelengths have made it possible to distinguish fields in components of clouds at different temperatures and to investigate conditions for grain alignment (Hildebrand et al. 1999). Comparisons with observations of Zeeman splitting have made it possible to describe changes in field inclinations (e.g., Brogan et al. 1999). These expanding scientific opportunities have attracted a growing community of observers.

This paper is intended to serve as an introduction to far-infrared polarimetry for those entering the field. We wish to provide observers, including those using facility instruments, with an outline of the basic procedures involved in polarization measurements and with guidelines for analyzing and interpreting the results, that is, with a review of effects within a source that may influence polarized emission and must therefore be taken into account as one seeks to turn data into science.

The discussion of observing procedures is based primarily on experience with instruments developed at the University of Chicago. We will include topics shared with far-infrared photometry and hence familiar to some potential readers. Since the technology is still developing rapidly, we will not discuss instrumentation. We present only a schematic design of a generic instrument. Our current instruments are well documented (Platt et al. 1991; Schleuning et al. 1997; Dowell et al. 1998). We limit the discussion of observing techniques to those for single telescopes. Higher spatial resolution, for bright, compact objects, can be achieved with antenna arrays at wavelengths as short as 1.3 mm (e.g., Rao et al. 1998) and will soon become possible at even shorter wavelengths with the Submillimeter Array (SMA). The observing techniques for interferometric polarimetry are considerably different and merit their own primer, but many of the principles involved in analyzing the results are the same as those discussed here.

The discussion of analysis guidelines will deal with effects encountered in nearly all applications of far-infrared polari-

¹ University of Chicago, Enrico Fermi Institute and Department of Astronomy and Astrophysics, 5640 Ellis Avenue, Chicago, IL 60637; roger@oddjob.uchicago.edu, johnv@oddjob.uchicago.edu.

² Department of Physics, University of Chicago.

³ Universities Space Research Association, NASA Ames Research Center, MS T3B, Moffett Field, CA 94035; jdavidson@mail.arc.nasa.gov.

⁴ SETI, NASA Ames Research Center, MS 245-6, Moffett Field, CA 94035; dotson@cygnus.arc.nasa.gov.

⁵ California Institute of Technology, Mail Code 320-47, 1200 East California Boulevard, Pasadena, CA 91125; cdd@submm.caltech.edu.

⁶ Department of Physics and Astronomy, Dearborn Observatory, Northwestern University, Evanston, IL 60208-2900; g_novak@nwu.edu.

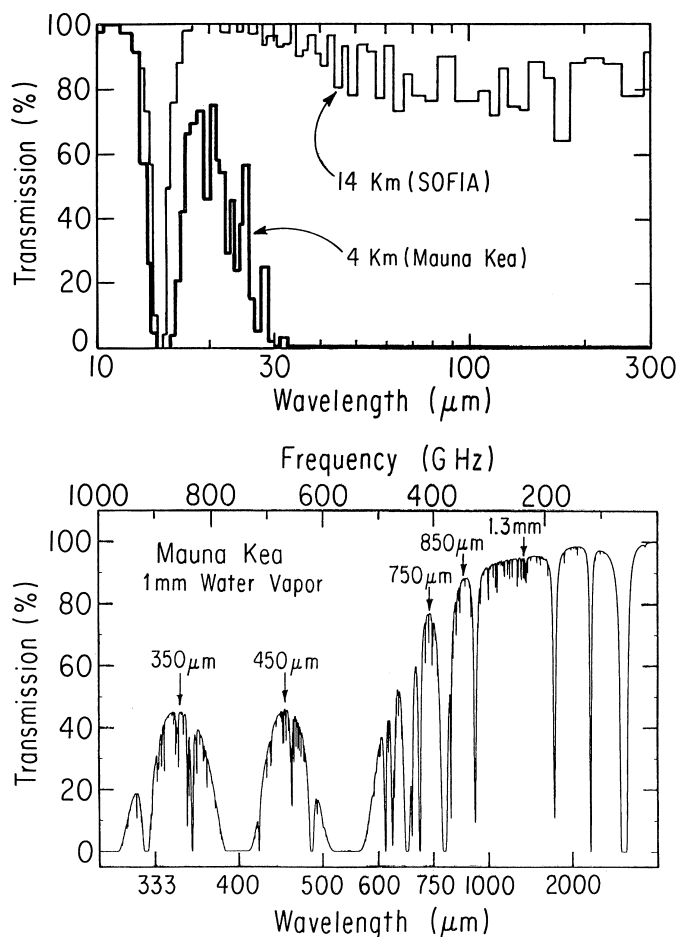


FIG. 1.—Atmospheric transmission at 14 km (KAO, SOFIA) and 4.2 km (Mauna Kea at 1 mm precipitable water vapor). The arrows in the lower panel mark the centers of “atmospheric windows” commonly used in ground-based submillimeter observations. Atmospheric conditions in these windows are often monitored by the optical depth, τ , at 225 GHz: $\tau(225 \text{ GHz}) = 0.05$ corresponds to ~ 0.8 mm precipitable water vapor.

metry. Whether the goal of an observation is to determine the effects of magnetic fields on the formation of an individual star or on the structure of a whole galaxy, one must take account of absorption, temperature variations, turbulence, and field inclinations. One must also seek to determine the domains within a source responsible for the polarized emission. In this connection we discuss the importance of measuring and analyzing polarization spectra.

We begin with a brief discussion of the relevant emission spectra.

2. SOURCE SPECTRUM AND BACKGROUND FLUX

The peaks of the emission spectra of Galactic clouds usually fall within the range $\sim 40\text{--}300 \mu\text{m}$, a range that was accessible from the Kuiper Airborne Observatory (KAO)

and will soon again become accessible from SOFIA (the Stratospheric Observatory for Infrared Astronomy). “Atmospheric windows” at 350, 450, 750, 850 μm , and beyond (Fig. 1) make it possible to do polarimetry at submillimeter wavelengths from ground-based telescopes at dry mountaintop sites. The various heating and cooling processes in a typical cloud generally produce a spectrum corresponding to a range of temperatures (e.g., Fig. 2; Sievers et al. 1991).

When analyzing an emission spectrum, one must be concerned at the short-wavelength end with optical depth effects and at the long-wavelength end with contributions from molecular line emission, free-free emission, synchrotron emission, and, beyond ~ 3 mm, electric dipole emission (Draine & Lazarian 1998). In ground-based and airborne observations, however, the preponderance of the far-infrared flux entering a polarimeter is not from any of these effects in the astronomical source but rather from the thermal emission of the local atmosphere and telescope. Moreover, the background flux is noisy because of fluctuations in the atmospheric transmission and emission. We begin our technical discussion with the problems of subtracting the background and reducing the noise.

3. OBSERVING PROCEDURES

3.1. Removing the Background

Procedures for removing the local background vary according to the circumstances and objectives of the observations. For observations within the Earth’s atmosphere, all these procedures involve comparisons of signals at source points with signals at neighboring reference points chosen, where possible, to be off the source. The problem is essentially the same for polarimetry as for photometry except

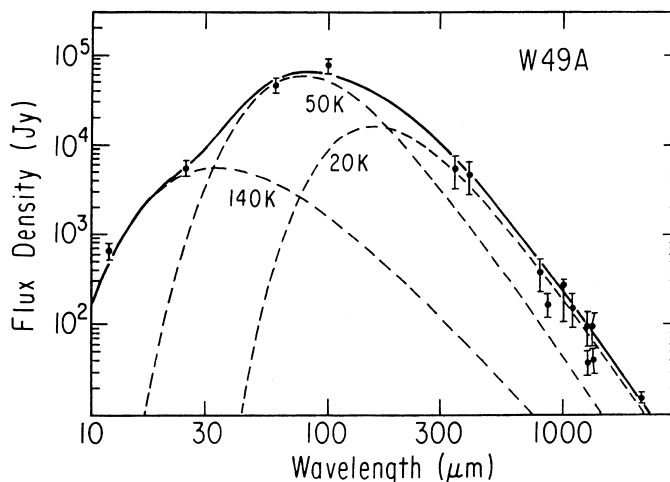


FIG. 2.—Total flux spectrum and derived temperature components of the molecular cloud W49A. Adapted from Sievers et al. 1991. (Area sampled includes warm component in core.)

that the polarized component of the flux is much smaller than the total flux in comparison to the background.

We consider first an instrument with a single detector. We further simplify the discussion by postponing to the next section any consideration of the noise except to point out that the noise due to atmospheric fluctuations will be reduced if the comparison of source and reference fluxes can be done rapidly.

Let $F(x)$ be the flux from a point, x , on the source, and let $F(y1)$ and $F(y2)$ be the fluxes from two reference points at equal and opposite displacements from x . Assume that the background at x is given approximately by the average of the backgrounds at $y1$ and $y2$. The net flux from the source will then be

$$I(x) = G \left\{ F(x) - \frac{[F(y1) + F(y2)]}{2} \right\}, \quad (1)$$

where G is a calibration factor which one need not evaluate unless the goal is an absolute flux measurement. (For arrays of detectors one must evaluate relative values of the G 's to correct for the different efficiencies of the individual sensors.)

In order to switch between points more rapidly than would be possible by moving the whole telescope, one "chops" (or "wobbles") a mirror, usually the secondary mirror, located between the telescope primary mirror and the instrument. The chopping frequency (typically ~ 15 Hz on the KAO; ~ 3 Hz on the Caltech Submillimeter Observatory [CSO], ~ 8 Hz at the James Clerk Maxwell Telescope [JCMT], ~ 3 Hz for the Viper telescope at the South Pole) must be fast enough so that $1/f$ noise from the atmosphere and from the detector system is not a dominant factor. (Do not imagine, however, that chopping removes the slow components of the atmospheric fluctuations in a measurement of polarization. That problem lies ahead.) The achievable chopping frequency depends on mechanical constraints and on the angular chopping amplitude, Δ (measured on the sky). Even at low frequencies, Δ is limited by aberrations and by the necessity to keep the entire moving beam on the telescope primary. The "beam" is the portion of the sky seen by a detector. Its diameter is typically $\sim \lambda/\mathcal{D}$, where \mathcal{D} is the diameter of the primary mirror of the telescope. The total separation, $D = 2\Delta$, of the two beams on the sky is the "chopper throw."

The usual procedure is to chop between two points, say, x and $y1$, at equal and opposite angles, Δ , to the optic axis of the telescope and then to move ("nod") the telescope so as to chop between x and $y2$, again in directions equidistant from the optic axis. (The points $y1$ and $y2$ are separated by a distance $2D = 4\Delta$.) The chopper runs continuously throughout the process at a fixed frequency and a fixed throw (typically $\sim 6'$ for the CSO, $\sim 8'$ for the KAO, $\sim 30'$ for Viper, $\sim 2'$ for the JCMT, but shorter throws for

compact objects). To the extent allowed by the inertia and driving torques of the chopping mechanism, the displacement follows a square wave. The following steps are illustrated in Figure 3:

1. Put one beam on the source point, x . Call it the "left" beam, l , regardless of the actual chopping direction. The reference point $y1$ will then be in the "right" beam, r .
2. Chop (~ 100 cycles) between x and $y1$ and integrate the difference, $(l_x - r_{y1})$.
3. Nod the telescope so as to put r on the source point, x . The reference point $y2$ will then be in the left beam.
4. Chop between $y2$ and x and integrate the difference $(l_{y2} - r_x)$. At this point one could repeat the cycle. But to remove "offsets" (see step 8) and improve efficiency it is better to do the following:
5. Repeat step 4 (no nod).
6. Nod to starting position (l at x).
7. Repeat step 2.
8. Derive the net signal from the results of the above steps:

$$\begin{aligned} & (l_x - r_{y1}) - (l_{y2} - r_x) - (l_{y2} - r_x) + (l_x - r_{y1}) \\ &= 4 \left\{ F(x) - \frac{[F(y1) + F(y2)]}{2} \right\}. \end{aligned}$$

The symmetric procedure outlined in these steps removes the DC components of the background emission from the sky and telescope and removes gradients ("offsets") with a linear time dependence. (This would not be true if one returned to step 1 after step 4.)

9. Repeat the whole cycle as often as necessary to get an adequate detection. (In the case of polarimetry, one steps the analyzer to the next position between each repetition.)

At this point we have an uncalibrated net signal as measured by a single detector. In an array with many detectors, one can follow the same procedure except that it becomes necessary to find relative coefficients, G (eq. [1]), to correct for differences in the response of the various detectors. That is usually done by moving the array on the sky and comparing the signals for different detectors on the same source points, a process called "flat-fielding." The process is described by Dowell et al. (1998).

3.2. Sky Noise

Now consider a real measurement with noise due to fluctuations in atmospheric emission and transmission. The strip-chart trace of the signal $(l - r)$ for a faint source will not follow smooth displacements as in the idealized curve of Figure 3, but will appear, instead, as noisy oscillations with drifts in the baseline and jagged peaks as in the top three traces of Figure 4. [We will return to this figure in connec-

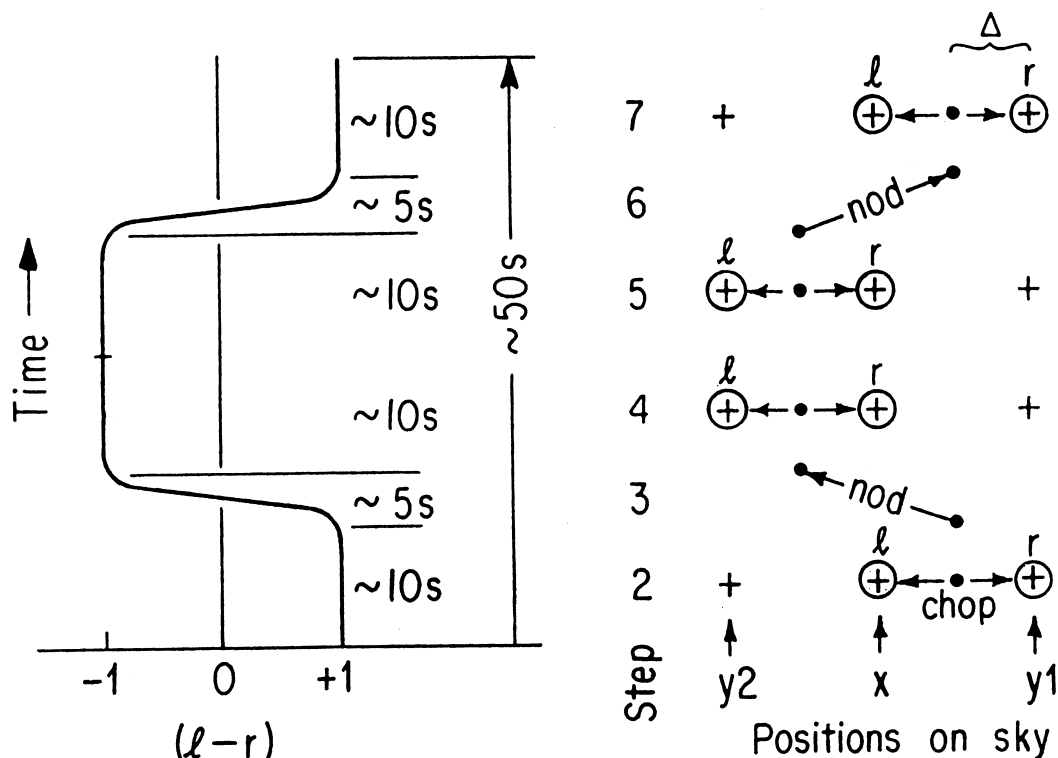


FIG. 3.—Sketch of a strip-chart trace of the signal $(l - r)$ for a single photometric cycle following the steps outlined in § 3.1 and assuming negligible noise. The positions of the optic axis (dots) and beams (small circles) are shown at the right for each step.

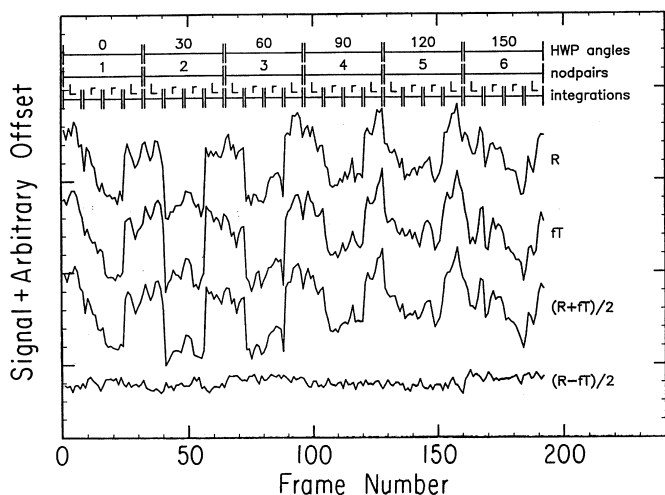


FIG. 4.—Strip-chart record (Dowell et al. 1998) of frames accumulated during a single file (six steps of the half-wave plate) during an observation of the source IRC +10216 ($F_v = 30$ Jy). Each point on a curve is 1 frame, the fundamental unit of stored data accumulated for 2 cycles of the chopping secondary at the CSO (0.6 s). The T -frames (one component of polarization) have been multiplied by a normalization factor, f , to bring them to the same scale as the R -frames (the other component). Correlated sky noise is evident in R and T as well as their sum (third trace: the total photometric signal). The correlated noise is removed by taking the difference ($R - fT$) (bottom trace). The steps of the observation are shown at the top (cf. Fig. 3).

tion with polarization signals (§ 3.3), but the trace labeled “ $(R + fT)/2$ ” is the sum of the signals for two orthogonal components of polarization and is thus exactly equivalent to an ordinary photometric signal ($\times \frac{1}{2}$).] This is an example of excess “sky noise” caused by changes in the background emission between the left and right beams. For an instrument with a single detector there is little one can do about the atmospheric noise except to repeat the measurement for many cycles. But with an array of detectors one can take advantage of the fact that the atmospheric noise is correlated over the whole focal plane and can be removed by taking the difference between signals in center pixels on the source and edge pixels off the source (Jenness, Lightfoot, & Holland 1998). Figure 5 shows an application of this technique. Notice the importance of determining whether the edge pixels are completely off the source.

An alternative method permits removal of the background and sky noise while scanning “on the fly” without nodding. This procedure is especially valuable for sources larger than the array (§ 3.5). If one scans, say, from right to left, across a source while chopping in the scanning direction along a row of detectors, the signal from the source will appear in each detector first in the left beam and then in the right. (By considering a scan along a row of detectors we simplify the discussion, but other scan directions can be

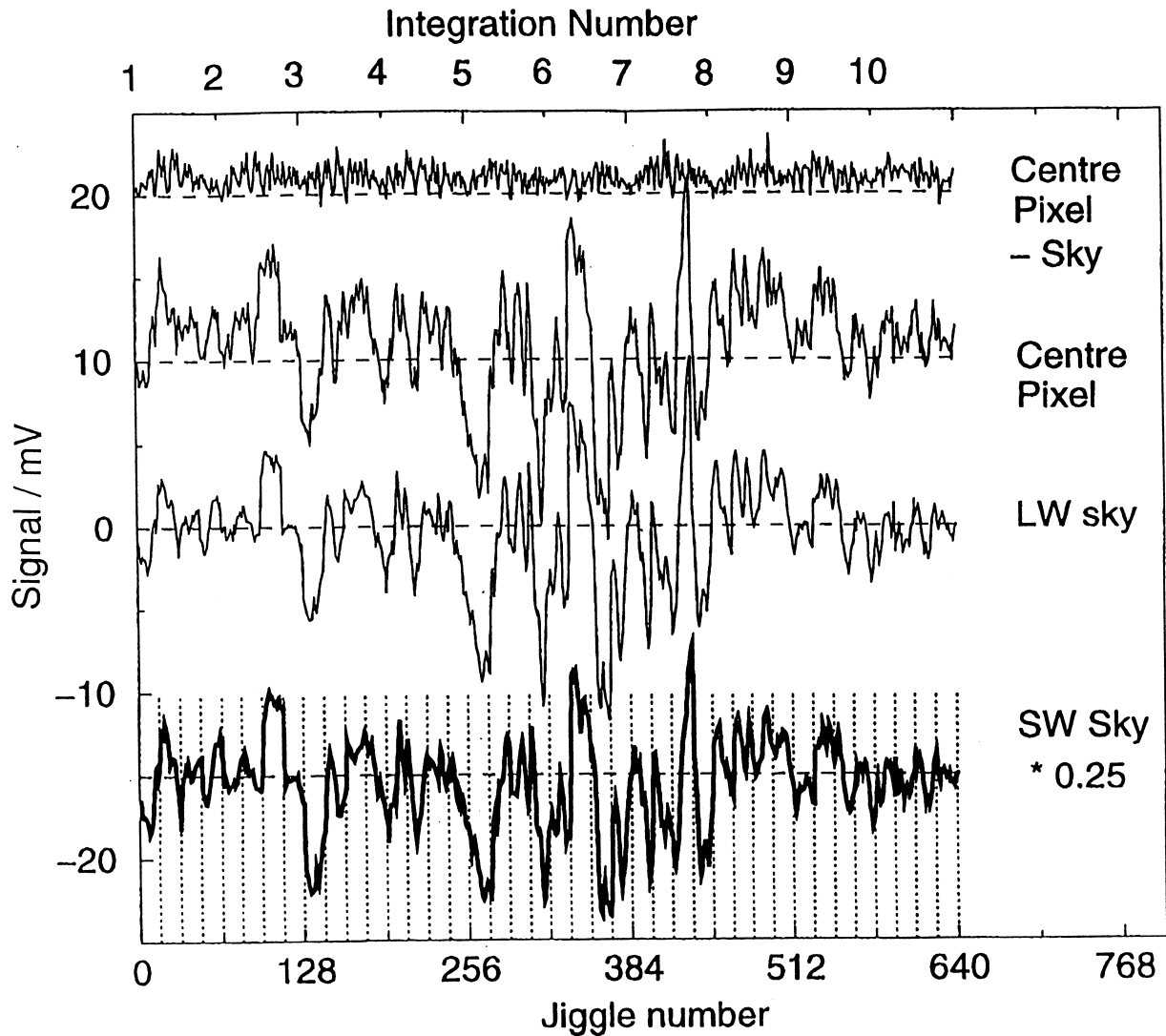


FIG. 5.—Removal of correlated atmospheric noise in an observation of comet Hale-Bopp using the SCUBA camera at the JCMT (Jenness, Lightfoot, & Holland 1998). The center two traces show the signals in the center (“on-source”) pixel and in the outer ring (“sky”) pixels (both at $850\ \mu\text{m}$). The top trace shows the net signal (on-source minus sky). The low level ripple in the net signal is the result of a sequence of small displacements (“jiggling” or “dithering”) repeating every 64 samples. The bottom trace (showing the same correlated noise) gives the sky signal ($\times \frac{1}{4}$) at $450\ \mu\text{m}$ during the same time interval.

used to advantage.) A plot of the signals ($l - r$) versus time will then have the form shown in the upper panel of Figure 6. The sky noise appears simultaneously in the whole row of detectors while the source moves through the detectors sequentially. The total signal, $S_d(t)$, in detector d at time t is

$$S_d(t) = G_d \{ F[x_d(t)] + N(t) \} + C_d, \quad (2)$$

where G = detector gain; F = source flux as a function of sky position, $x_d(t) = x_l(t - \Delta t_d)$, where Δt_d = time to scan from pixel 1 to pixel d ; $N(t)$ = correlated sky noise; and C = constant offset (residual background or electronic offset).

The noise is removed by adjusting $N(t)$ to minimize the difference between the net signals registered by pixels along

the scan. The resulting solution for $S_d(t) - N(t)$ is shown in the lower panel of the figure. To avoid inverting a large matrix, one can use an iterative solution solving sequentially for the terms $S_d(t)$, $N(t)$, C_d , and G_d , a process that should be viable for large arrays.

3.3. Polarization Signals

We turn now to the measurement of polarization signals. For those measurements one can take advantage of the fact that the fluctuations in atmospheric emission and transmission are correlated for orthogonal components of polarization, and if the signals for those components are measured simultaneously the noise is removed by taking the difference

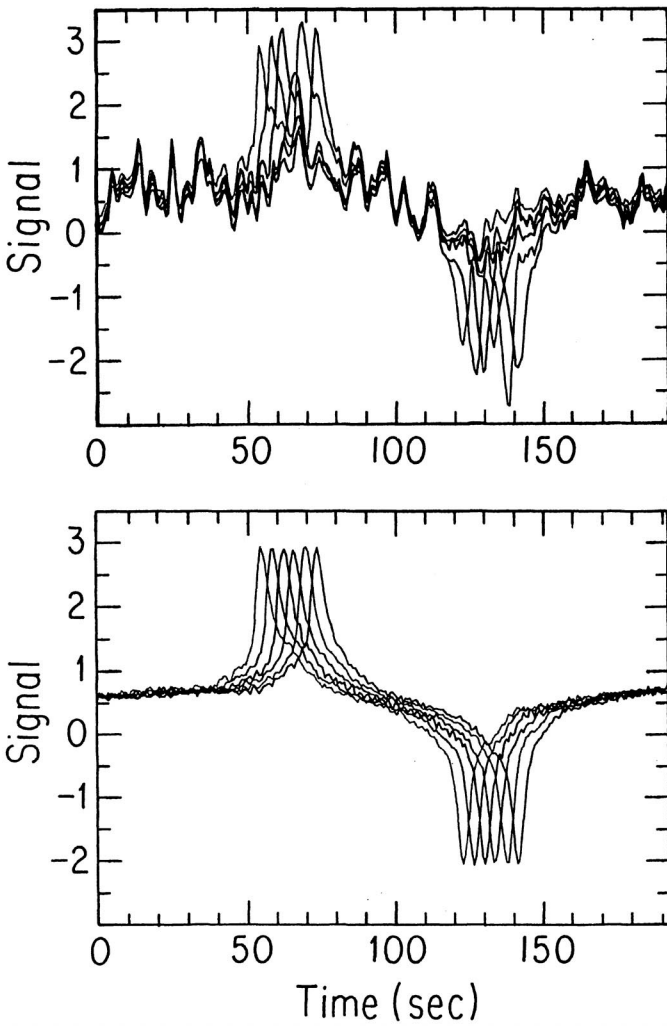


FIG. 6.—The signal, $(l - r)$ (arbitrary units), for a scan on-the-fly along a row of six detectors in the University of Chicago instrument, Hertz. (Source: OMC-1; scan rate: $5'' \text{ s}^{-1}$; chop throw: $5/5$; chop rate: 2.7 Hz.) The raw signal is shown in the upper panel. The signal from the source appears first in the left beam and then in the right beam of each detector with a time lag equal to the beam separation divided by the scanning rate. The coherent noise appears in each detector with no time lag. The lower panel shows the signals after processing to remove the correlated noise as described in § 3.2.

(e.g., Hildebrand et al. 1984; Dowell et al. 1998). That technique can be applied either when chopping between fixed points or when chopping on the fly. (The SCUBA polarimeter detects a single component. The noise is normally reduced by taking the difference between on- and off-source signals.)

We consider first the detection of a single component with a single detector, then two components with one detector for each component, and finally two components in two arrays of detectors.

If a fine grid of parallel wires (wire separation of less than $\sim \lambda/5$) is placed across the path of the radiation ahead of the

detectors, the component of the radiation with the E vector parallel to the wires will be reflected: the component perpendicular to the wires will be transmitted and can be coupled to a detector. If the grid is rotated, the signal in the detector will vary with the rotation angle, θ , according to the degree and direction of the polarization; i.e., the grid will serve as a “polarization analyzer.” The degree of polarization is

$$P = \frac{(I_{\max} - I_{\min})}{(I_{\max} + I_{\min})}. \quad (3)$$

The direction of the polarization is given by the angle, $\phi(\max)$, of the E vector on the sky, at which the intensity, $I(\phi)$, is a maximum. Notice that the intensity is also a maximum at $\phi(\max) + n\pi$. The difference of $I(\theta)$ from its mean value, $\langle I(\theta) \rangle$, should vary as $\sin 2\theta$.

Instead of rotating a grid, one can rotate a half-wave plate ahead of a fixed grid. A rotation of the half-wave plate through an angle θ rotates the plane of the incoming radiation by 2θ , i.e., rotating the half-wave plate through an angle 2θ is equivalent to rotating a grid by 4θ . Thus the variation in intensity should be given by

$$I(\theta) - \langle I(\theta) \rangle = A \sin [4(\theta - \delta)], \quad (4)$$

$$\frac{[I(\theta) - \langle I(\theta) \rangle]}{\langle I(\theta) \rangle} = P \sin [4(\theta - \delta)], \quad (5)$$

where

$$\delta = \frac{1}{2}(\phi - \alpha + \gamma - \chi) \quad (6)$$

is a phase angle depending on ϕ , the angle of the E vector on the sky; α , the rotation angle of the sky with respect to the instrument (measured clockwise from the vertical to celestial north); γ , the angle of the instrument rotator; and χ , the angle of the incident polarization that will produce $\delta = 0$ when $\gamma = 0$. For sign conventions, see Platt et al. (1991). (For the SCUBA polarimeter, mounted at the Nasmyth focus of the JCMT with no instrument rotator, the rotation of the sky with respect to the instrument depends on the elevation and parallactic angle.)

The relationship between the angle, ϕ , of the polarization in the plane of the sky and the angle of the half-wave plate, $\theta_{\max} (= \pi/8 + \delta)$, such that $I = I_{\max}$, depends on the orientation of the axis of the half-wave plate and the orientation of the polarizing grid within the instrument. Although this relationship can be computed if the relevant angles are accurately and reliably known, the safest practice is to make a laboratory measurement using a chopped source and a

wire grid ahead of the instrument. If the grid is oriented to transmit only radiation in the plane corresponding to the vertical direction on the sky, and if the rotator is set at $\gamma = 0$, then the function $[I(\theta) - \langle I(\theta) \rangle] / \langle I(\theta) \rangle$ found by rotating the half-wave plate will give the value of θ_{\max} (and χ) for $\phi = 0, \alpha = 0$.

Ideally, this function should have the form given by equation (5) and shown in the curve at the bottom of Figure 7, with two maxima and two minima for a rotation of θ through 180° . But because of the noise due to atmospheric fluctuations, the actual result, especially for faint sources at $\lambda \leq 350 \mu\text{m}$, can be an almost random pattern of points as in the top two panels of the figure, each recorded for a single component.

An optical design for simultaneous detection of two orthogonal components of polarization is shown schematically in Figure 8 (e.g., Hildebrand et al. 1984). In this design, a fixed wire grid following the half-wave plate is inclined at 45° to the optic axis. The component parallel to the wires is reflected to one detector array (the R array), and the other component is transmitted to another array (the T array). The “polarization signal” is then

$$S(\theta) = \left[\frac{(R - T)}{(R + T)} \right]_\theta. \quad (7)$$

Fluctuations in atmospheric transmission affect R and T by equal factors and hence leave $S(\theta)$ unchanged. Fluctuations in atmospheric emission (unpolarized) produce correlated excursions in R and T that are removed in the numerator of equation (7) when taking the difference. These fluctuations are generally small compared to the denominator, $(R + T)$. As we have seen, however, the noise in $(R + T)$ can also be reduced (§ 3.1).

The effectiveness of this scheme is shown in the bottom trace of Figure 7. Another illustration of noise removal by this process is provided by Figure 4 showing strip-chart traces of the signal $(l - r)$ for an unpolarized source. The traces show the individual components, their sum, and their difference. The signals for one component, T , have been multiplied by a normalization factor (called f in Fig. 4) to bring R and T into the same scale.

(Note to § 3.3: One might suppose that P could be measured by rotating an analyzer without chopping to obtain the polarized flux, $P \times F$, and then dividing by a value of the flux, F , obtained from a photometric map. But as we have said, the preponderance of the flux reaching the detectors is not from the source but from the local background, and that flux will become polarized by the instrumental polarization [e.g., $\sim 1\%$ due to the dichroic tertiary of SOFIA] to produce a total polarized flux much greater than that due to the source. Hence this approach does not appear to be realistic.)

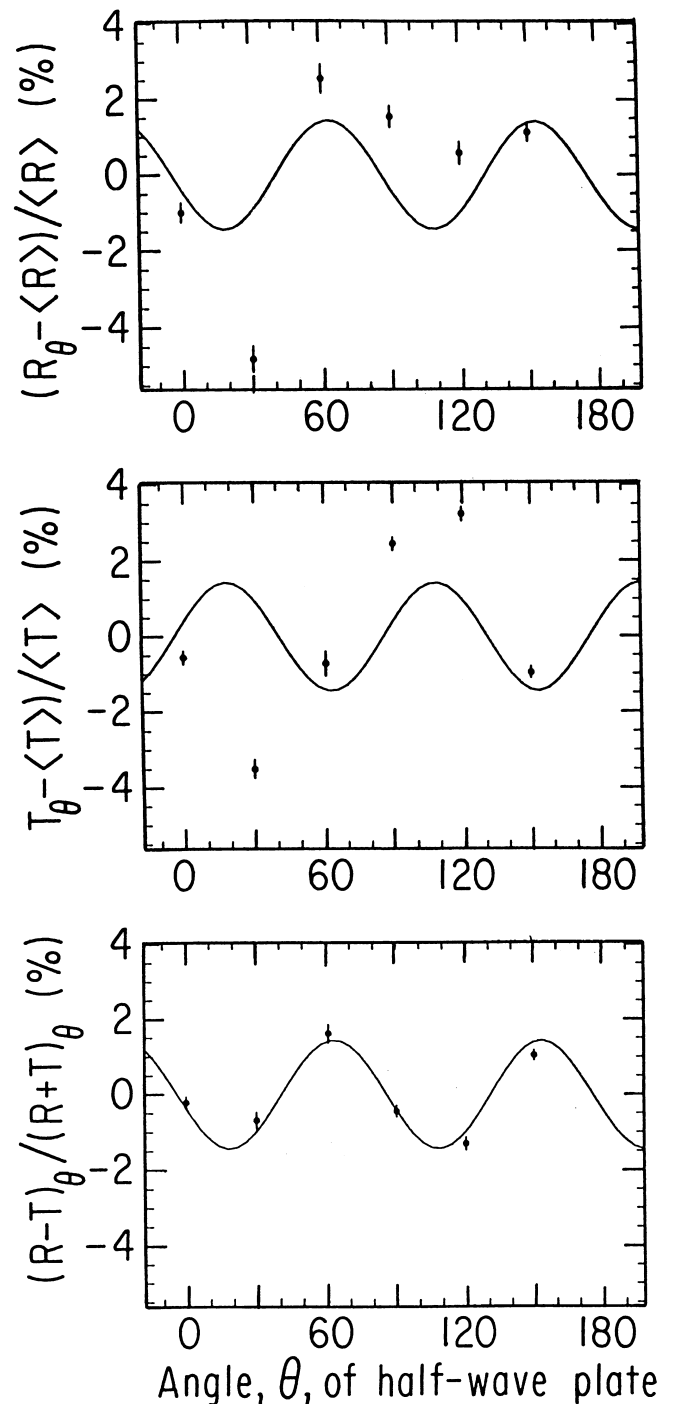


FIG. 7.—Effect of atmospheric variations on polarization signals. Panels *a* and *b* show results obtained by analyzing separately the data for two orthogonal components of polarization, R and T , for a single rotation of the half-wave plate through 180° in 30° steps. With a stable atmosphere one would expect $[R_\theta - \langle R \rangle] / \langle R \rangle$ and $[T_\theta - \langle T \rangle] / \langle T \rangle$ to fit curves of the form $A \cos [4(\theta - \delta_0)]$ and $A \cos [4(\theta - \delta_0) + \pi]$; (two maxima and two minima for a rotation through 180°). As is evident, no satisfactory fits are possible. Panel *c* shows the fit obtained when the data for the two components are subtracted to form $(R - T)_\theta / (R + T)_\theta$.

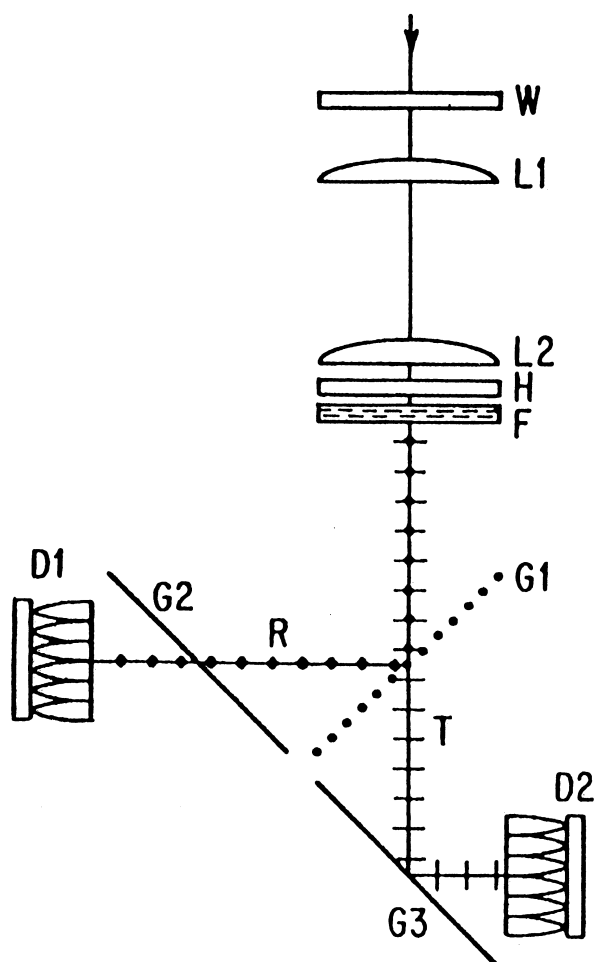


FIG. 8.—Schematic diagram of the optics for a polarimeter. Radiation enters through vacuum window, W, passes through lens, L1, at an image of the sky and through a second lens, L2 at an image of the primary. L2 reimages the sky at the detector arrays, D1 and D2. A rotating half-wave plate, H, close to L2 rotates the plane of polarization. A spectral filter, F, behind H defines the passband. A wire grid, G1, reflects component *R* parallel to the wires and transmits component *T* perpendicular to the wires. Component *R* is then transmitted by a second grid, G2, and enters detector array, D1. Component *T* is reflected by grid G3 and detected by array D2. One measures the quantity $(R - T)/(R + T)$ as a function of the angle of rotation, θ , of the half-wave plate.

3.4. Stokes Parameters, Instrumental Polarization, Errors

We have not yet taken account of spurious components of polarization introduced by the telescope, by the polarimeter itself, or by unknown polarization in the reference beams. To contend with these effects one must know how to add polarization vectors and then find an observing strategy to measure and remove components unrelated to the source. One adds familiar polar or axial vectors by putting the tail of one at the head of the other and drawing the resultant. But a polarization vector does not have a head or a tail: it is unchanged by a 180° rotation. The resultant of

two unit polarization vectors at right angles has a magnitude of zero, not $\sqrt{2}$. The method of dealing with such vectors was invented by Sir George Stokes in 1852 (see Stokes 1901).

Consider a polarization ellipse as in Figure 9 where the radius at a given angle represents the amplitude of the electric field and where ξ is the angle of polarization with respect to a coordinate system in the polarimeter. Let β be a number (not a geometrical angle) such that the semimajor and semiminor axes are $a \cos \beta$ and $a \sin \beta$. Then $I(\max) = a^2 \cos^2 \beta$ and $I(\min) = a^2 \sin^2 \beta$. Using these expressions we have

$$\begin{aligned} P &= \frac{[I(\max) - I(\min)]}{[I(\max) + I(\min)]} \\ &= \frac{(a^2 \cos^2 \beta - a^2 \sin^2 \beta)}{(a^2 \cos^2 \beta + a^2 \sin^2 \beta)} \\ &= \cos^2 \beta - \sin^2 \beta \\ \text{or } P &= \cos 2\beta. \end{aligned} \quad (8)$$

For a single light wave, *i*, define Stokes parameters as follows:

$$I_i = a^2, \quad (9a)$$

$$Q_i = a^2 \cos 2\beta \cos 2\xi, \quad (9b)$$

$$U_i = a^2 \cos 2\beta \sin 2\xi, \quad (9c)$$

$$V_i = a^2 \sin 2\beta. \quad (9d)$$

Actual light is a superposition of many waves with independent phases. The Stokes parameters for the entire beam are

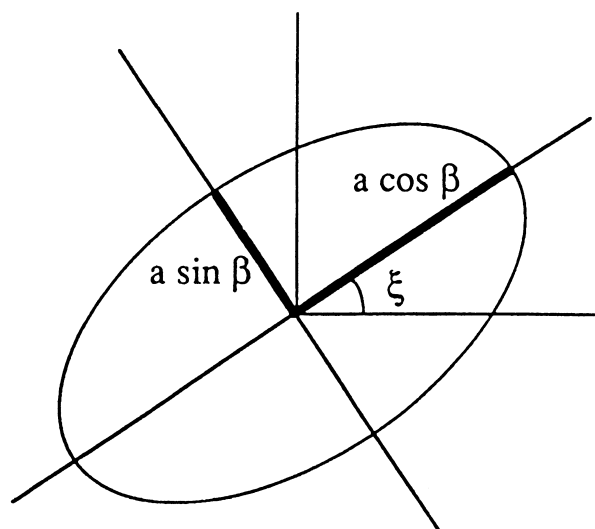


FIG. 9.—Polarization ellipse (polar plot of *E* vector amplitudes). The angle, ξ , is the direction of polarization with respect to a reference frame in the instrument

given by the sums

$$I = \Sigma I_i, \quad Q = \Sigma Q_i, \quad U = \Sigma U_i, \quad V = \Sigma V_i, \quad (9e)$$

where

$$I^2 \geq Q^2 + U^2 + V^2 \quad (9f)$$

and where the two sides of equation (9f) are equal only for a 100% polarized beam. For an unpolarized beam, $I = a^2$ and $Q^2 = U^2 = V^2 = 0$.

The fourth Stokes parameter, V , specifies the degree of circular polarization and is not relevant to this discussion of plane-polarized light. But do not conclude, because we ignore it here, that V is unmeasurable or unimportant (e.g., Martin & Angel 1976; Baily et al. 1998; Bower & Backer 1998; Sault & Macquart 1999).

These four parameters completely characterize the intensity and state of polarization of a beam of radiation. A key property of the parameters is that the resultant polarization for radiation passing through an interstellar cloud or an instrument can be obtained by simply adding the parameters for each cloud layer or each component of the optical system of the telescope and instrument.

For many purposes the data can conveniently be analyzed in terms of reduced Stokes parameters defined by

$$q = \frac{Q}{I} = P \cos 2\xi, \quad (10a)$$

$$u = \frac{U}{I} = P \sin 2\xi. \quad (10b)$$

Notice that the quantity

$$q^2 + u^2 = P^2(\cos^2 2\xi + \sin^2 2\xi) = P^2 \quad (11)$$

is invariant with respect to the orientation of the ellipse. If ξ changes while the reference frame remains fixed in the polarimeter, then points in the q - u plane will move on a circle of radius P . The direction of polarization with respect to the reference frame is given by

$$\xi = \frac{1}{2} \tan^{-1} \left(\frac{u}{q} \right). \quad (12a)$$

The angle ξ is related to the phase angle, δ , of equations (4), (5), and (6) and to θ_{\max} , the angle of half-wave plate such that $I = I_{\max}$, by

$$\xi = 2(\delta - \theta) + \frac{\pi}{4} = 2(\theta_{\max} - \theta). \quad (12b)$$

The observed polarization is due to the combined effects of the source, s , the telescope t , and the polarimeter, p . The values of q and u for these components are additive when their sum is $\ll 1$ as in all cases considered here (but not $\ll 1$ for strongly polarized synchrotron sources). Hence the measured Stokes parameters can be written as

$$q = q_s + q_t + q_p, \quad u = u_s + u_t + u_p. \quad (13)$$

If the polarimeter is fixed with respect to the telescope and the sky rotates, then the measured Stokes parameters, q_i , u_i , at a point, i , at sky rotation, α_i , will be given by

$$q_i = P_s \cos 2(\xi_i - \alpha_i) + (q_t + q_p), \quad (14a)$$

$$u_i = P_s \sin 2(\xi_i - \alpha_i) + (u_t + u_p). \quad (14b)$$

Equations (14a) and (14b) are the parametric representation of a circle of radius, P_s , centered at a point $(q_t + q_p)$, $(u_t + u_p)$, representing the combined effects of the sky and telescope. We thus have the magnitude, $P_s = [(q_i - q_t - q_p)^2 + (u_i - u_p - u_t)^2]^{1/2}$, and angle, $\xi_s = \frac{1}{2} \tan^{-1} [(q_i - q_t - q_p)/(u_i - u_p - u_t)]$, of the source polarization for a pixel on the axis of rotation.

When an instrument with an array of detectors remains fixed with respect to an altitude-azimuth telescope, there is the complication that as the sky rotates the pixels move with respect to the sky. (Only a pixel on the axis of rotation remains fixed on the sky.) To deal with that problem one rotates the instrument so as to follow the sky rotation. The telescope then rotates with respect to the sky and the instrument. One must solve separately for the polarization due to the telescope and that due to each pixel in the array.

Consider first the telescope polarization. If one rotates the polarimeter to follow the rotation of the sky, then points in the q - u plane will describe a circle of radius equal to P_t centered at $(q_s + q_p)$, $(u_s + u_p)$ as illustrated in Figure 10 ($P_t \approx$ constant over all pixels). In the example shown in the figure, P_t is due primarily to reflection from the dichroic tertiary mirror of the KAO telescope. As is evident, however, P_t can be measured accurately, especially when one combines the results for every object in a series of observations.

Using a sequence of translations and 90° rotations of the instrument, one can obtain enough information to solve for the Stokes parameters of the source and the associated errors at every observed point in the sky. The procedure does not rely on any calibration source of known polarization.

The best fit to the six required Stokes parameters (q_s , q_p , q_t , u_s , u_p , u_t) is determined through a multiple linear regression (Platt et al. 1991). Such regressions also return the errors for each of these parameters in the diago-

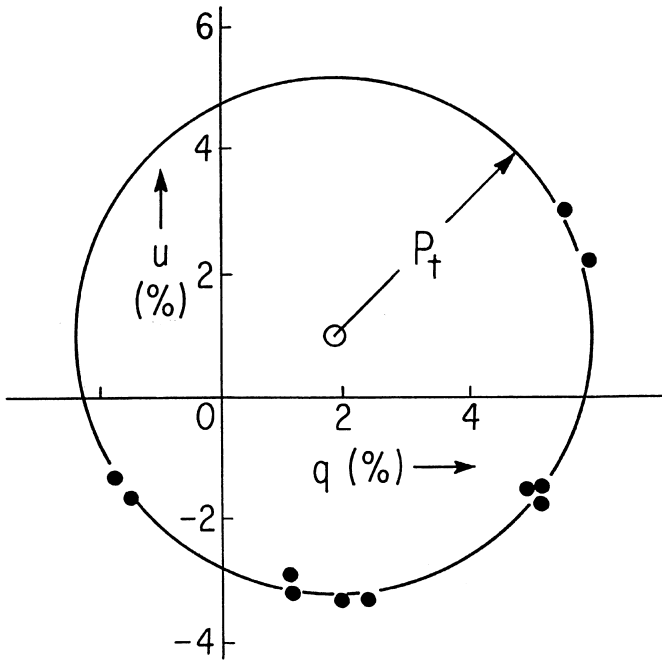


FIG. 10.—Points in the q - u plane as measured during a flight of the KAO. The polarimeter was rotated to follow the sky. The points trace a circle of radius P_t centered at $(q_s + q_p), (u_s + u_p)$. (Data for W3, a northern object, were taken during an eastbound flight: hence large sky rotation.) If the instrument had remained fixed with respect to the telescope, the points would have traced a circle of radius P_s centered at $(q_t + q_p), (u_s + u_p)$.

nal values of the covariance matrix (e.g., see Bevington & Robinson 1992). Given the expressions for P (eq. [11]) and ξ (eqs. [12a] and [12b]) standard error propagation (for $P/\sigma \gg 1$) yields

$$\sigma_P \approx \frac{1}{P} \sqrt{(q^2 \sigma_q^2 + u^2 \sigma_u^2)} \approx \sigma_q \text{ if } \sigma_q \approx \sigma_u, \quad (15a)$$

$$\sigma_\xi \approx \frac{1}{2P^2} \sqrt{(q^2 \sigma_u^2 + u^2 \sigma_q^2)} \approx \frac{\sigma_P}{2P} \quad (15b)$$

(σ_ξ in radians). As P/σ decreases, the errors become increasingly non-Gaussian (see § 4.2).

3.5. Polarized Flux in the Reference Beams.

We began with a procedure to remove the background due to emission from local sources. It is a procedure that is valid only if the positions, y_1 and y_2 , of the reference beams are, in fact, off the source. But that condition is often not satisfied for extended sources. Polarized flux in the reference

beams is a potential source of large systematic errors and is the main reason to reflect before crediting your polarization map. In the case of photometry one can at least say that the flux at point x is a measured level above (or below) the average of that at points y_1 and y_2 . In the case of polarimetry it is not only the flux but also the direction and degree of polarization at y_1 and y_2 that may be unknown.

There is no justification for assuming that the polarization is low where the flux density is low. The opposite is more often true (e.g., Matthews & Wilson 2000; Davis et al. 2000). A further difficulty is that the reference beams are often in regions where there are no large-scale photometric maps of adequate resolution. What has usually been the only choice is to get the best available flux maps, however inadequate, assume that the reference flux is polarized at least as strongly as in any portion of the uncorrected polarization map, and calculate the corresponding limits, $\Delta P +$ and $\Delta P -$, as one rotates the assumed polarization vectors for the reference beams. For discussions of this fallback procedure, see Novak et al. (1997) and Schleuning et al. (1997).

To solve the problem properly one must make long scans. The scans may consist of measurements at a series of points across the source while chopping and nodding and advancing the half-wave plate at each point, but it is more efficient to make a series of scans on the fly, advancing the half-wave plate between each scan, recording the data in bins no larger than a resolution element, and then analyzing the result as if done at discrete points.

Consider a scan in the x -direction: let

D = chopper throw,

$f(x)$ = true distribution of the desired quantity

(I , Q , or U),

$g(x)$ = measured distribution as given by

$$g(x) = f(x) - \frac{1}{2}[f(x + D) + f(x - D)]. \quad (16a)$$

(See eq. [1] and Fig. 11.)

Now choose a point x_0 believed to be at least a distance D from the source. Measure $g(x_0 - D)$, $g(x_0)$, $g(x_0 + D)$, $g(x_0 + 2D)$, ..., $g(x_0 + nD)$. If point x_0 is, in fact, off the source by $\geq D$, then one should find $g(x_0 - D) = g(x_0) = 0$. If point $x_0 + nD$ is at least a distance D beyond the other side of the source, then one should find $g(x_0 + mD) = g[x_0 + (m + 1)D] = 0$ when $m \geq n$.

Rearranging equation (16a) we have

$$f(x + D) = 2[f(x) - g(x)] - f(x - D). \quad (16b)$$

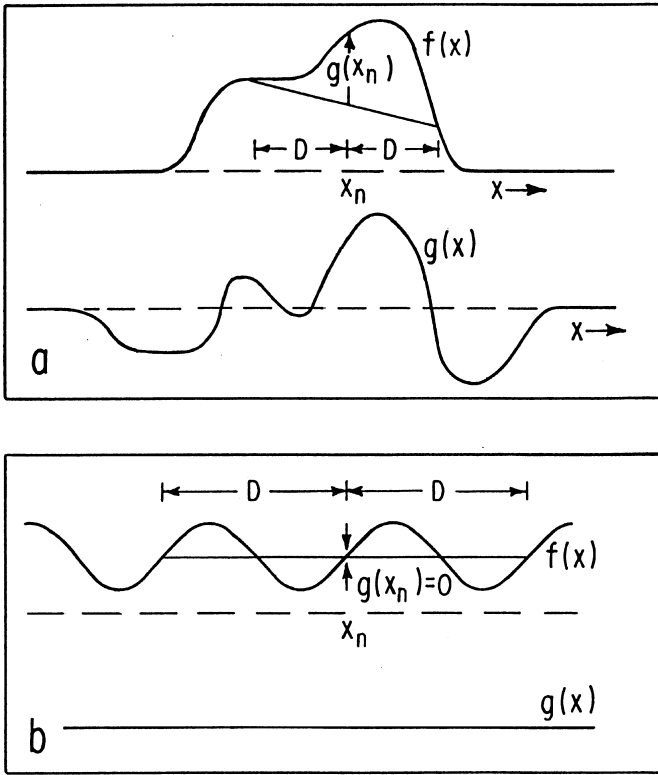


FIG. 11.—Scan of an extended object. The curve $f(x)$ represents the true distribution of the desired quantity (I or Q or U). The curve $g(x)$ represents the measured distribution. The graphical construction shows the relationship of $g(x)$ to $f(x)$. The lower panel illustrates the failure of $g(x)$ to detect features in $f(x)$ of period $\rightarrow D$.

Applying equation (16b) repeatedly we have

$$\begin{aligned}
 f(x_0) &= 0, \\
 f(x_0 + D) &= 0, \\
 f(x_0 + 2D) &= 2[0 - g(x_0 + D)] - 0 = -2g(x_0 + D), \\
 f(x_0 + 3D) &= 2[-2g(x_0 + D) - g(x_0 + 2D)] - 0, \\
 f(x_0 + 4D) &= 2[-2g(x_0 + D) - 2g(x_0 + 2D) \\
 &\quad - g(x_0 + 3D)] + 2g(x_0 + D) \\
 &= -6g(x_0 + D) - 4g(x_0 + 2D) \\
 &\quad - 2g(x_0 + 3D). \\
 f(x_0 + nD) &= -2 \sum_{i=1}^{n-1} (n-i)g(x_0 + iD) \quad (17)
 \end{aligned}$$

To limit the random walk of the errors, now adjust the measured values of $f(x_0 + iD)$, within errors, to satisfy the condition $f(x_0 + mD) = 0$ for $m \geq n$.

A limitation to the procedure outlined above is that its

sensitivity for features in $f(x)$ approaches zero wherever those features approach a periodicity of length D (or $D/2$, etc.; see Fig. 11b). This problem can be solved by repeating the measurement with different values of D . For a discussion of the problem and of techniques to optimize the analysis, see Haslam (1974) and Emerson, Klein, & Haslam (1979).

3.6. Noise

We conclude the discussion of polarization techniques with a summary of noise sources. The relative importance of these sources depends on weather, wavelength, source intensity, detector characteristics, chopping amplitude, and optics. (For further discussion, see Mather 1982 and Duncan et al. 1995.)

1. *Detector/amplifier noise*.—Typically white noise but increasing as $1/f$ at low frequencies. (Not a significant factor with modern detectors.)
2. *Photon noise*.—White component of noise from the sky due to statistical fluctuations in photon arrival times. (Generally below sky noise for observations within the Earth's atmosphere for chopper throws greater than $\sim 1'$, but the fundamental noise limit once sky noise is removed.)
3. *Atmospheric noise*.—This noise is relatively severe at $\lambda \leq 450 \mu\text{m}$. Here we summarize the comments on atmospheric noise already discussed in § 3.1:

a) *Emission* ("sky noise").—Background noise due to changes in atmospheric emission at source and reference points (adds equal increments to the signals R and T). This noise can be reduced by reducing the chopping amplitude. On extended objects, however, low chopping amplitudes exacerbate the problem of unknown polarization in the reference beams. Sky noise is removed from the difference, $(R - T)$, in the numerator of the expression for the polarization signal (eq. [7]) by simultaneous detection of two orthogonal components of polarization. This noise is removed from both the numerator and the denominator, $(R + T)$, by processing on-the-fly scans as described in § 3.1.

b) *Transmission*.—Changes in the received signal due to atmospheric opacity. These changes affect the signals R and T by equal factors and are effectively removed from the polarization signal, $(R - T)/(R + T)$, by simultaneous detection of two orthogonal components.

4. *Pointing noise*.—Noise generated by drifting of the source with respect to the center of a detector especially in the case of bright compact sources. If the arrays for the two components of polarization are not accurately aligned, or if only one array is used, then the pointing error will introduce noise in the polarization signal wherever there are gradients in the flux density or polarization.

4. ANALYSIS GUIDELINES

To interpret a map of polarization or a polarization spectrum, $P(\lambda)$, in terms of a particular investigation, one must take into account conditions within the source that may influence the results. We present a sample map (Fig. 12: Orion; Dowell et al. 2001) and discuss how such a map can be affected by opacity, turbulence, temperature variations, changes in mean field inclination, and conditions favoring or inhibiting grain alignment.

4.1. Polarization Maps

A polarization map typically shows polarization E vectors overlaid on flux density contours. It may also include a gray scale to indicate the magnitude of the polarized flux, $P \times F$. In a uniform field $P \times F$ is proportional to the integral along the line of sight of the density of aligned grains weighted by the Planck function, by the emissivity, and by the polarizing efficiency of the grains.

In most cases one can assume that the E vectors are perpendicular to the magnetic field. The spin axes of the grains (the short axes) precess rapidly about the direction of the field, B , and components of the spin perpendicular to B are suppressed by magnetic damping (paramagnetic relaxation). The long axes, and hence the E vectors of the emitted radiation, then tend to be perpendicular to B . To visualize the configuration of the aligning field as projected on the sky, it is useful to redraw the map with the vectors rotated through 90° as in Figure 13. The vectors have been drawn the same length to avoid any implication that the length of a “ B vector” gives information about the strength of the field. In most cases a 90° rotation of the vectors gives a valid representation of the projected field direction.

Streaming of gas with respect to the grains tends to align the spin axes of the grains in the plane perpendicular to the relative motion. If the streaming is due to ambipolar diffusion of neutral gas across a magnetic field and thus through clouds of charged dust grains tied to the field, both streaming and magnetic damping will tend to put the long axes of the grains perpendicular to B (Roberge, Hanany, & Messenger 1995). But streaming *along* field lines, for example, in supersonic outflows, tends to put the long axes parallel to B . Lazarian (1997) has discussed the dependence of streaming alignment on grain shape, streaming velocity, and streaming direction with respect to the field.

In one known case, the core of Sgr B2, the polarization is due to selective absorption of background radiation by a cold foreground layer (Dowell 1997). For that object the vectors at $\lambda \leq 100 \mu\text{m}$ are parallel to the field in the absorbing layer. The realization that Sgr B2 is an exceptional case came from comparing results at different wavelengths.

4.2. Distributions in Degrees of Polarization

Data on distributions in degrees of polarization at different wavelengths are valuable in planning observations and crucial in interpreting the results. Figure 14 shows histograms for measurements at 60, 100, and $350 \mu\text{m}$ (Hildebrand et al. 1999). At the time this paper is being written this is the best available guide to the distributions in this range of wavelengths. There are several limitations, however, in using this figure as a guide. Two of the limitations have to do with the data sample: (1) Most of the measurements were made in the envelopes of giant molecular clouds. It is likely that other types of objects would produce different results. (2) There is only partial overlap between the objects observed at the three wavelengths. Hence the figure does not provide a valid comparison of the distributions characteristic of the different wavelengths even for the one type of source. A subset of the data restricted to areas in which there is a complete overlap does show the same trend toward a decrease in P with λ in this range of wavelengths.

This trend, however, does not hold for all environments and does not continue to longer wavelengths. In the Orion molecular cloud, the results at $800 \mu\text{m}$ (Aitken et al. 1997) and $1300 \mu\text{m}$ (Leach et al. 1991) show that in this object the polarization spectrum rises again beyond $350 \mu\text{m}$, but the available data are still too scattered to permit more than the qualitative conclusion that $P(800 \mu\text{m})$ and $P(1300 \mu\text{m})$ are both significantly greater than $P(350 \mu\text{m})$. The results for OMC-3 at $850 \mu\text{m}$ (Matthews & Wilson 2000) show a similar and better defined increase in P beyond $350 \mu\text{m}$ (Fig. 15).

Two other limitations in using the distributions of Figure 14 as a guide have to do with non-Gaussian errors. (3) We have included only measurements giving nominal values of $\geq 3 \sigma$ significance. This restriction tends to remove points with low values of P because they are less likely to give 3σ detections. (4) Values of P can only be positive (or, by convention, only negative in the case of polarization by absorption: § 4.4). If one accepts values of low significance, there will be measurements giving values of order 1σ even where the true values are close to zero. This again tends to skew the distribution away from low values. The nominal distribution will be altered as discussed by Rice (1947; see also Serkowski 1958; Wardle & Kronberg 1974; Simmons & Stewart 1985; and Leahy & Fernini 1989). If P_M is the measured value, then a corrected value, P_0 , is given, to first approximation, by

$$P_0 = \sqrt{(P_M^2 - \sigma^2)}. \quad (18)$$

For many applications equation (18) provides a statistically adequate correction to the distribution where $P_M > 2 \sigma$.

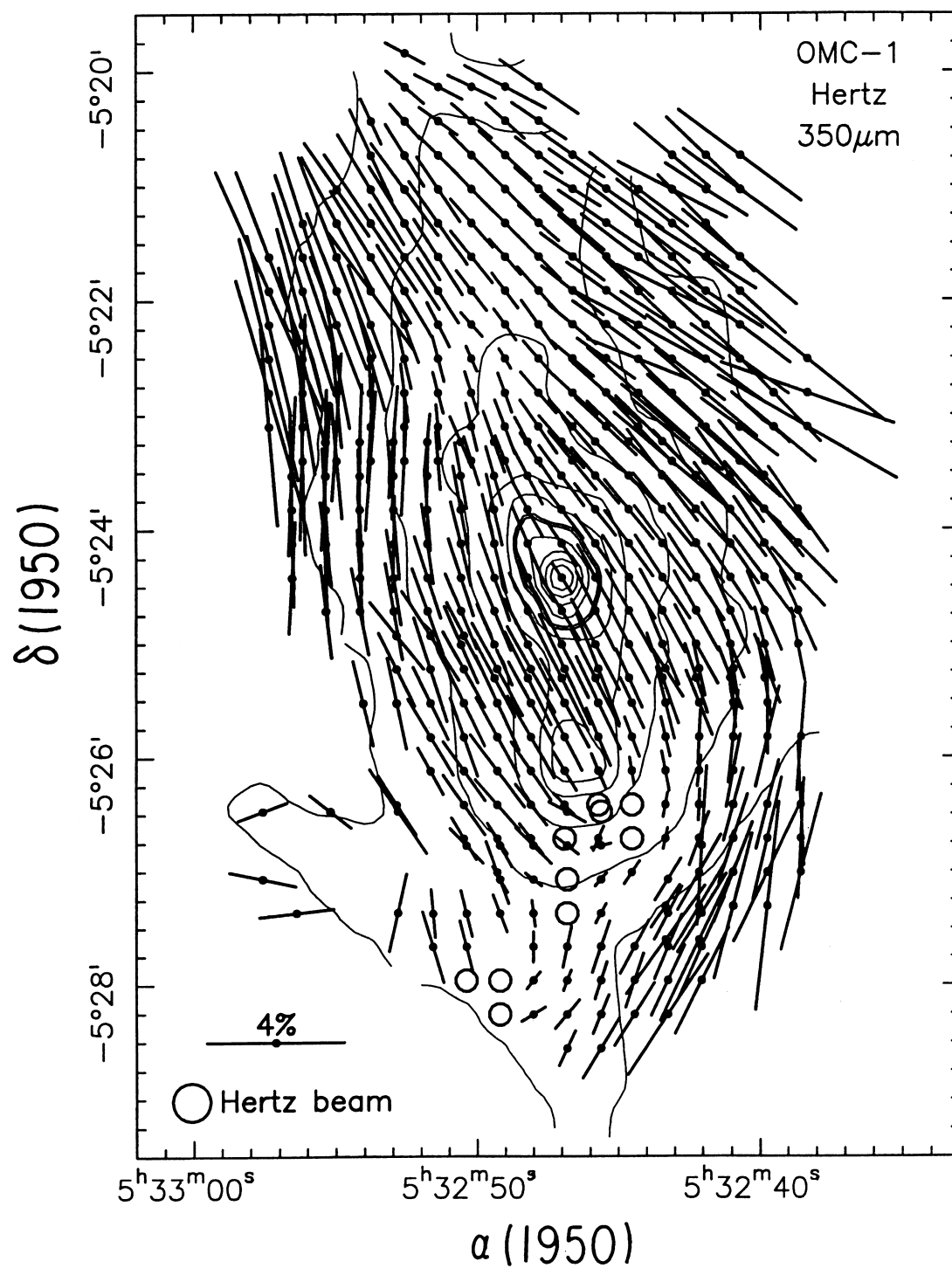


FIG. 12.—Polarization map of Orion (CSO observations with Hertz at $350\mu\text{m}$: Dowell et al. 2001). The vectors ($P/\sigma \geq 3$) show the direction of the maximum electric field. Open circles denote upper limits, $P + 2\sigma < 1\%$. The contours show the total flux distribution ($R + T$) as measured during the polarimetry with levels of 5%, and 10%–90% in 10% intervals.

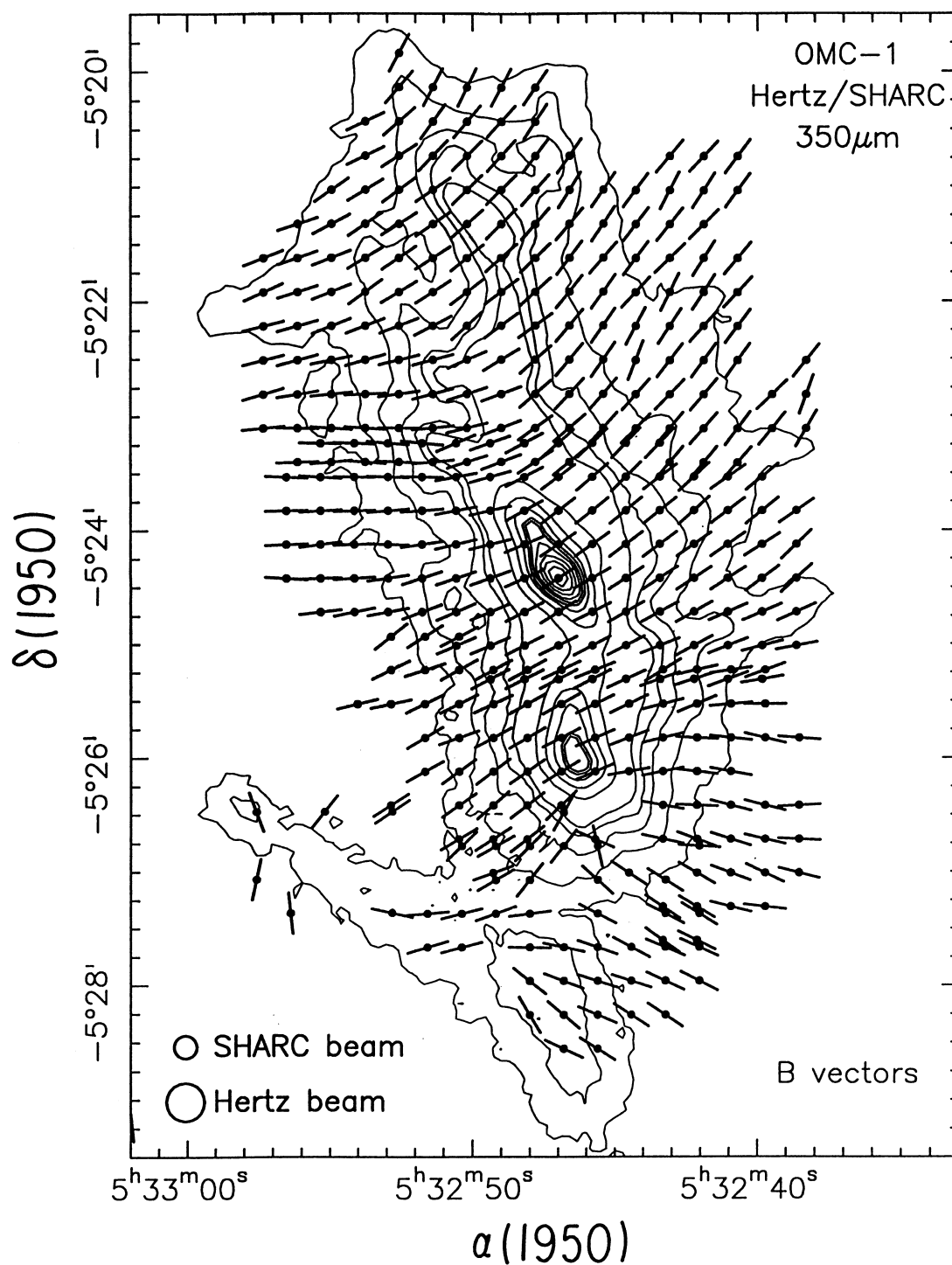


FIG. 13.—Orion map. Same data as in Fig. 12 but with vectors rotated 90° to show the inferred direction of the magnetic field. All vectors drawn to the same length. The contours show flux densities measured at the same wavelength, $350\mu\text{m}$, with the photometer SHARC (Lis et al. 1998).

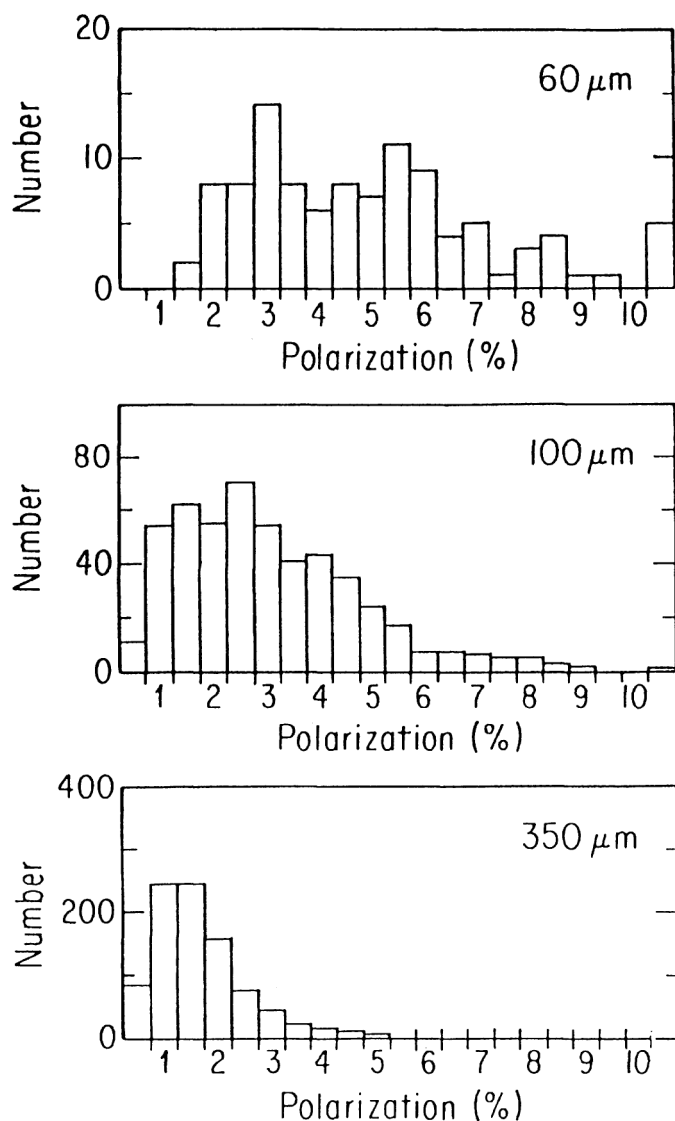


FIG. 14.—Distributions in degrees of polarization, P , at 60, 100, and 350 μm for measurements with $P > 3\sigma$ (Hildebrand et al. 1999). The last bins at the right show the sums of all measurements with $P \geq 10\%$.

For $P_M > 3\sigma$ the corrections are less than 10% and can generally be ignored. We have verified that the *relative, median* values of the distributions in Figure 14 are not significantly altered by accepting values of low significance with or without applying corrections.

4.3. Field Strength: Field Inclination

The first thing to realize when analyzing a map of polarization is that one should *not* assume any direct correlation between the degree of polarization and the strength of the field. The degree of polarization depends on many factors including the uniformity of the aligning field, the inclination of the field to the line of sight, the optical depth, the local

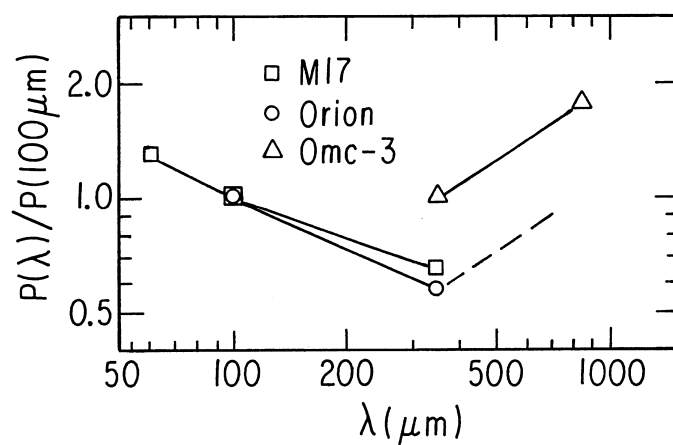


FIG. 15.—Polarization spectra of three molecular clouds. The results for M17 and Orion (Hildebrand et al. 1999) are normalized at 100 μm . Observations by Aitken et al. (1997) and Leach et al. (1991) indicate an increase in $P(\lambda)$ beyond 350 μm but results are scattered (hence dashed line). The results for OMC-3 at 350 μm (this paper) and 850 μm (Matthews & Wilson 2000) are normalized at 350 μm . The 850 $\mu\text{m}/350 \mu\text{m}$ comparison is restricted to the $40''$ region centered on the cloud axis, a region where the errors are small and the ratios approximately constant.

environment, and the shapes, dielectric functions, and magnetic susceptibilities of the dust grains. There must be some minimum field for magnetic alignment of grains, but as yet there is no observed correlation between field strength and degree of polarization. It may be that the fields in Galactic clouds are generally strong enough to produce nearly optimum alignment of all the grains that are susceptible to alignment (see discussion by Jones 1989).

One can make indirect estimates of field strength by combining polarimetry with data from other observations (e.g., Dotson 1996; Schleuning 1998). Chandrasekhar & Fermi (1953) estimated the strength of the field in the arms of the Galaxy by combining data on the angular dispersion of the polarization vectors with data on line widths and densities in the same regions (but see § 4.6 for a precaution in applying this technique). Their estimate (a few μG) has been verified by measurements of Faraday rotation and Zeeman splitting. In denser regions the values, chiefly from Zeeman measurements, range from $\sim 10 \mu\text{G}$ in diffuse clouds to as much as $\sim 10 \text{ mG}$ in molecular clouds (Myers & Goodman 1988).

Zeeman measurements give field strengths along the line of sight. In dense regions the measurements are made in absorption on the near side of a cloud. Polarimetry samples dust alignment through the depth of a cloud as projected on the sky. Nevertheless, one can use comparisons of Zeeman and linear polarization maps to infer changes in field inclination. An example is provided by M17. In that object, Zeeman measurements (Brogan et al. 1999) show a strong line-of-sight field ($\sim 450 \mu\text{G}$) along a north-south line through the intensity peak where the polarization vectors

(Dotson 1996; Dotson et al. 2000) are short and a weak line-of-sight field in the eastern half of the cloud where the polarization vectors are long. We infer that the field is nearly along the line of sight at the north-south line and turns toward the plane of the sky at points farther to the east.

In some cases one can use observations of degrees of polarization to infer limits on the inclination of the field. Among hundreds of measurements ($\geq 3 \sigma$) made with the University of Chicago polarimeter, Stokes, at $100 \mu\text{m}$, only one is above 10% (Fig. 14). One can thus infer that where the degree of polarization at $100 \mu\text{m}$ is strong, say, greater than 6%, the field must be more nearly parallel than perpendicular to the plane of the sky (e.g., Novak et al. 1997).

4.4. Optical Depths in Homogeneous Clouds

The effect of optical depth on degrees of polarization is easily discussed in the case of homogeneous clouds. We leave to the next section the case of clouds with heterogeneous temperature structures.

Consider the absorption of a beam of unpolarized light traveling in the z -direction through a cloud layer containing aligned grains, where the absorption, τ_x , is greatest for the component of the light with the E vector in the x -direction and least, τ_y , for the component in the y -direction. The polarization, P_a , by selective absorption in the cloud layer will be

$$P_a = \frac{[\exp(-\tau_x) - \exp(-\tau_y)]}{[\exp(-\tau_x) + \exp(-\tau_y)]} \quad (19a)$$

$$= -\tanh\left[\frac{(\tau_x - \tau_y)}{2}\right] \quad (19b)$$

$$\approx -\frac{(\tau_x - \tau_y)}{2} \left[\text{if } \frac{(\tau_x - \tau_y)}{2} \ll 1 \right]. \quad (19c)$$

By convention P_a is negative, indicating polarization by absorption.

The polarization, P_e , by emission from the same cloud layer will be

$$P_e = \frac{\{[1 - \exp(-\tau_x)] - [1 - \exp(-\tau_y)]\}}{\{[1 - \exp(-\tau_x)] + [1 - \exp(-\tau_y)]\}} \quad (20a)$$

$$\approx \frac{(\tau_x - \tau_y)}{(\tau_x + \tau_y)} \quad [\text{for } (\tau_x - \tau_y) \ll 1]. \quad (20b)$$

Let

$$\Delta\tau = (\tau_x - \tau_y), \quad (21a)$$

$$\tau = \frac{(\tau_x + \tau_y)}{2}. \quad (21b)$$

Then

$$P_a \approx -\frac{\Delta\tau}{2}, \quad (21c)$$

$$P_e \approx -\frac{P_a}{\tau}. \quad (21d)$$

The transmitted radiation is polarized in a plane perpendicular to that of the emitted radiation. For low values of τ , P_a is proportional to $\Delta\tau$ and hence to τ , but P_e is constant.

Notice that equation (21d) holds only where $\tau \ll 1$ and where P_e and P_a are measured at the same wavelength. It is rarely true that P_e and P_a can actually be measured at the same wavelength. One measures P_a in the optical or near-infrared in clouds that are tenuous enough that one can see background stars: one measures P_e at wavelengths in the far-infrared in clouds that are dense enough to provide significant thermal emission. To make comparisons at different wavelengths one must estimate the dependence of P_e on λ using an assumed dielectric function for the grain material (van de Hulst 1957; Draine & Lee 1984; Hildebrand 1988). Strictly speaking, one must also assume a shape for the dust grains (e.g., Hildebrand & Dragovan 1995), but in the far-infrared, *relative* values of P_e at different values of λ are insensitive to the shape (Hildebrand et al. 1999).

It is sometimes useful to rewrite equation (20a) in terms of equations (21a) and (21b). The result is

$$P_e = \frac{e^{-\tau} \sinh(\Delta\tau/2)}{[1 - e^{-\tau} \cosh(\Delta\tau/2)]} \quad (22a)$$

or

$$P_e = \frac{e^{-\tau} \sinh(P_0 \tau)}{[1 - e^{-\tau} \cosh(P_0 \tau)]}, \quad (22b)$$

where P_0 is the polarization one would measure for $\tau \rightarrow 0$. If $P_0 \ll 1$ and if $\tau < \sim 1$, then equation (22b) reduces to the approximate expression

$$P_e \approx P_0 \left(1 - \frac{\tau}{2}\right). \quad (22c)$$

To first approximation $\tau \propto \lambda^{-\beta}$ where β is a constant of order 1–2. To this approximation one can rewrite equation

(19c) as

$$P_e \approx P_0 \left(1 - \frac{K}{\lambda^\beta}\right). \quad (22d)$$

4.5. Temperature Variations

Equations (19a)–(19c) for the τ -dependence of P_a are valid only for homogeneous clouds. Polarization by absorption will not obey equations (19a)–(19c) if there are variations along the line of sight in grain characteristics, in degrees of alignment, or in the direction of the aligning field. Polarization by emission (eqs. [20a] and [20b]) will be influenced by all of these variables and in addition by variations in temperature.

In discussing optical depth effects we have thus far ignored the difficulties in defining and measuring the optical depth itself. Before comparing a map of polarization vectors with a map of optical depths, one should investigate the origin of the τ -map. In most cases the first step in making such a map has been to compare flux densities, F , at two wavelengths (only) and to derive a value of the temperature, T , assuming

$$\frac{F(\lambda_1)}{F(\lambda_2)} = \left[\frac{(\lambda_1)}{(\lambda_2)}\right]^{-\beta} \left[\frac{\mathcal{B}(\lambda_1, T)}{\mathcal{B}(\lambda_2, T)}\right], \quad (23)$$

where $\mathcal{B}(\lambda, T)$ is the value of the Planck function at (λ, T) and $\lambda^{-\beta}$ is an assumed emissivity law (τ assumed $\ll 1$). The second step is to calculate $\tau(\lambda)$ from the derived value of T assuming

$$F(\lambda) = \mathcal{B}(\lambda, T)(1 - e^{-\tau}), \quad (24a)$$

or

$$\tau(\lambda) = \ln \left\{ \frac{1}{[1 - F(\lambda)/\mathcal{B}(\lambda, T)]} \right\}. \quad (24b)$$

The weakness of this procedure is immediately evident in Figure 2. There is no “correct” value of T . There is often, instead, a wide range of T -values. In regions displaced from cloud cores one sees a lower proportion of high temperature components than shown in this figure but still a considerable range of temperatures. What one would really like to know is the column density and the distribution of temperatures along each line of sight. Dust temperature distributions require photometric maps at wavelengths over the entire spectral range in which there is significant emission. The flux density distribution, $F(\lambda)$, at each point in the cloud must then be inverted to find the temperature distribution. Notice that one should not rely on a wavelength-dependent spectral index, $\beta(\lambda)$, to explain a spectrum, $F(\lambda)$, where the shape may be determined primarily by the pres-

ence of different temperature components and where the individual components may be characterized by temperature-dependent indexes, $\beta(T_i)$ (e.g., Sievers et al. 1991; Finkbeiner, Davis, & Schlegel 1999).

In many publications on this topic the equations are written in terms of the frequency, ν , instead of the wavelength, λ , and we will follow that practice. (Optical astronomers use wavelengths. Radio astronomers use frequencies. Far-IR and submillimeter astronomers are in between and must adapt to the practices at each end of the spectrum.)

In a cloud that is uniform and optically thin, the dust emission is given by

$$F(\nu) = N \left(\frac{\sigma}{L^2} \right) Q(\nu) \mathcal{B}(\nu, T) \quad (25a)$$

(e.g., Hildebrand 1983, 1988), where N = number of grains, σ = geometrical cross section of a grain = πr^2 , L = distance to the cloud, $Q(\nu)$ = grain emissivity, and $\mathcal{B}(\nu, T)$ = Planck function at (ν, T) .

In a real cloud with a range of temperatures equation (25a) becomes

$$F(\nu) = \frac{1}{L^2} \int n(T) \sigma Q(\nu) \mathcal{B}(\nu, T) dT, \quad (25b)$$

where $\int n(T) dT = N$. If we now define a dust-mass temperature distribution

$$M(T) = n(T) \rho v, \quad (25c)$$

where ρ = grain density and v = grain volume $\approx 4\pi r^3/3$, then

$$F(\nu) = \frac{3}{4L^2} \int \left[\frac{Q(\nu)}{(r\rho)} \right] M(T) \mathcal{B}(\nu, T) dT. \quad (25d)$$

The problem then is to solve for $M(T)$ given measurements of $F(\nu)$ at several wavelengths. This is one of many inverse problems in astronomy. Fortunately, there are good texts on the subject (e.g., Craig & Brown 1986; see also Jeffrey & Rosner 1986; and Li, Goldsmith, & Xie 1999).

When the temperature distribution is known one can estimate the optical depth associated with each temperature component. One should bear in mind that no amount of mathematical finesse can produce a valid temperature distribution without accurate measurements of $F(\nu)$ at many points in the spectrum from $h\nu/kT(\min) \gg 1$ to $h\nu/kT(\max) \ll 1$, where $T(\min)$ and $T(\max)$ are the temperatures of the coolest and warmest significant components of the emitting dust. Notice the importance of extending the measurements to the short-wavelength side of

the spectrum. If all the measurements are on the Rayleigh-Jeans tail of the distribution, one can fit the data with components at any temperature or any combination of temperatures T above $h\nu/k$.

With polarization maps at several wavelengths it becomes possible to investigate two aspects of cloud structure: (1) the large-scale three-dimensional configuration of the magnetic field, and (2) the nature of (possibly small scale) temperature domains in a heterogeneous cloud.

In some cases one sees systematic shifts in the angle of polarization as one observes at different wavelengths. In W3 for example (Schleuning et al. 2000) we find a clockwise shift of $\sim 15^\circ$ from 60 to 100 μm and another shift of $\sim 15^\circ$ in the same direction from 100 to 350 μm in the center portion of the cloud. One can assume a corresponding shift in the direction of the magnetic field between the warm core and cool outer regions of the cloud. In other cases (e.g., Orion) one sees no shift in position angle but a significant change in the degree of polarization.

4.6. Field Variations: Turbulence

Jones, Klebe, & Dickey (1992) have measured polarization by absorption, P_a , at 2.2 μm through long lines of sight with values of $\tau(2.2 \mu\text{m})$ from ~ 0.1 to ~ 10 . For a homogeneous cloud with low values of $(\tau_x - \tau_y)$ one would expect $P_a \propto \tau$ (eq. [19c]). For a medium with randomly oriented domains one would still expect P_a to increase with τ , but only at a rate corresponding to a random walk ($P_a \propto \sqrt{\tau}$) and at a magnitude depending on the step size. What they find is a slope of P_a versus τ that corresponds to approximately equal contributions from uniform and random components, and a step size corresponding to $\Delta\tau(2.2 \mu\text{m}) \approx 0.1$ [or $\Delta\tau(100 \mu\text{m}) \approx 0.002$, $\Delta A_v \approx 1$, $\Delta N_H \approx 3 \times 10^{21} \text{ cm}^{-2}$].

The patterns of vectors seen in most areas of current maps of polarized emission are remarkably smooth (e.g., Dotson et al. 2000). But this observation should not lead one to infer an absence of turbulence. Contributions from random components in domains along the line of sight tend to cancel each other, leaving only the polarization due to the uniform component of the aligning field (Zweibel 1996). Magnetic field strengths derived from the angular dispersion of the observed polarization vectors will be systematically overestimated if this effect is not taken into account (see Jones et al. 1992 and Myers & Goodman 1991).

Turbulence or other small-scale effects can, however, be observable when a large fraction of the polarized flux within a resolved region originates in a single domain. For example, Rao et al. (1998) have found large shifts in direction and amplitude between well-resolved domains (not necessarily turbulent domains) in Orion where the total flux is dominated by a small region close to the hot stars in the core. With adequate angular resolution, turbulence might

be observable in the envelopes of molecular clouds if the regions emitting the polarized flux do not overlap as projected on the sky. That condition could be satisfied if the aligned grains are concentrated in small regions around embedded stars. The wavelengths chosen for the observations should be short enough to favor detection of the relatively warm grains in those regions.

We consider next the effects on polarization spectra of such heterogeneous distributions of temperatures and polarization efficiencies.

4.7. Variations in Polarizing Efficiency: Polarization Spectra

An analysis of polarization data should take into account the likelihood that grains in different environments within a cloud may have different efficiencies for polarized emission. For example, magnetic alignment may be favored in regions near embedded stars or on the surfaces of clouds where direct exposure to stellar radiation may spin the grains to suprathermal rotational velocities thus increasing the time available for alignment by paramagnetic relaxation (Draine & Weingartner 1996; see also Purcell 1979 and Lazarian, Goodman, & Myers 1997). Alignment is apparently suppressed in cold dark clouds where the grains are shielded from stellar radiation (e.g., Arce et al. 1998). The environments may also differ in temperature (e.g., hot grains near embedded stars; warm grains shielded from the stars but in a medium warmed by the effects of turbulence, differential rotation, ambipolar friction, etc.; and cold surface grains removed from dynamical heating sources). Moreover, in a single environment, grains with different emissivities may

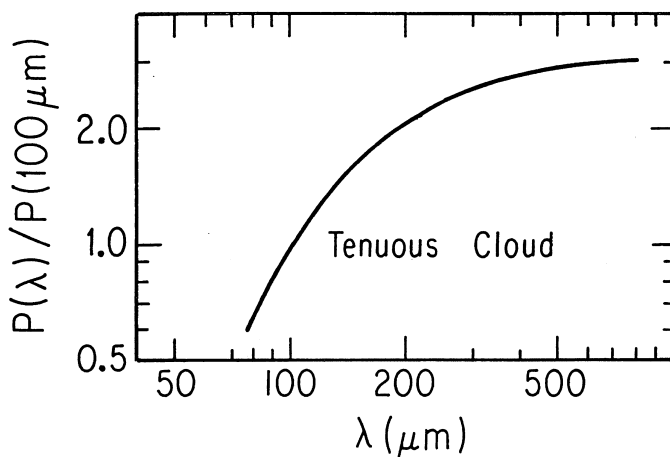


FIG. 16.—Polarization spectrum computed for a tenuous cloud ($\tau \ll 1$) exposed to the interstellar radiation field. Individual grain species A (aligned silicate) and B (unaligned graphite) are at temperatures $T_A = 15$ K and $T_B = 20$ K (Draine & Lee 1984). The curve is based on the dielectric functions of Draine (1985) assuming a volume fraction of $\frac{1}{4}$ for the graphite and assuming discrete graphite and silicate grains rather than composites.

have different temperatures and different polarization efficiencies. Wherever grains of different properties or grains in different environments contribute to the observed flux, the degree of polarization may depend on wavelength.

In all of the following we consider column densities such that $\tau \ll 1$. The dielectric functions of the commonly assumed grain materials at far-infrared and submillimeter wavelengths (but *not* at mid-infrared wavelengths) are such that

$$\frac{dP}{d\lambda} \approx 0 \quad (26)$$

for any single grain species in any single environment (Hildebrand et al. 1999). Polarization spectra of various shapes can be produced, however, when the observed emission is from mixtures of grains that differ both in their polarization efficiencies and in their emission spectra (Hildebrand et al. 1999).

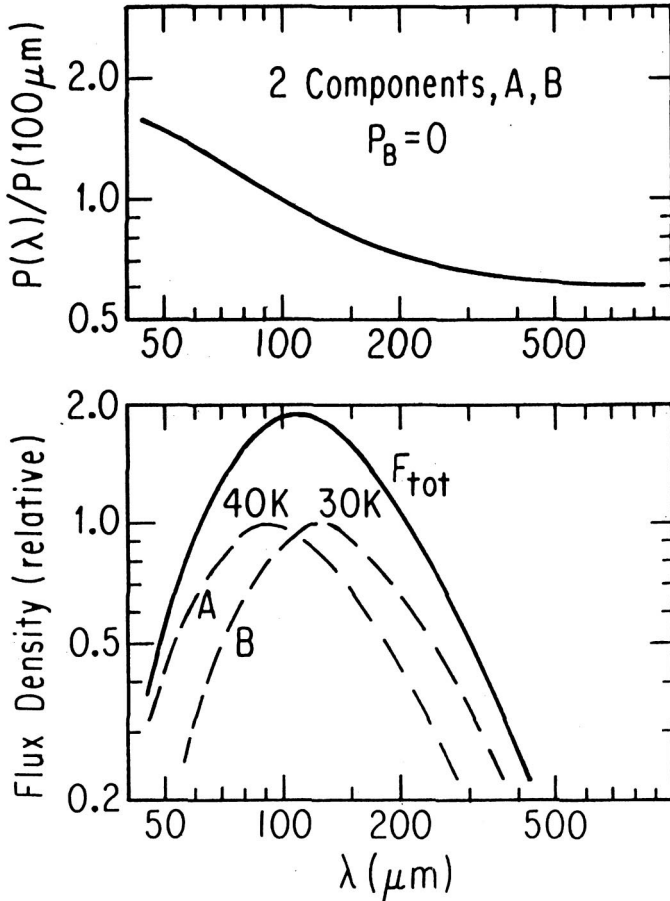


FIG. 17.—Polarization and flux spectra for a cloud with components at temperatures $T_A = 40$ K, $T_B = 30$ K where only the warmer component, A, contains polarized grains. (A and B contain identical grains in contrasting environments.) The peak flux densities are in the ratio 1:1. The flux spectra for the individual components have the form $\nu \mathcal{B}(\nu, T)$.

If the observed flux, F_{tot} , is the sum of n components, F_i , characterized by polarization efficiencies, P_i , then the polarization of the mixture will be

$$P_{\text{mix}}(\lambda) = \Sigma P_i X_i(\lambda), \quad (27)$$

where

$$X_i(\lambda) = \frac{F_i(\lambda)}{F_{\text{tot}}(\lambda)}. \quad (28)$$

From equation (25a) we have

$$F(\nu) \propto \left(\frac{\sigma}{L^2} \right) Q(\nu) \mathcal{B}(\nu, T) \quad (29a)$$

or

$$F_i(\nu) \propto V_i \left[\frac{Q(\nu)}{r} \right]_i \mathcal{B}(\nu, T), \quad (29b)$$

where $V = Nv$ = total volume of dust. The quantity (Q/r) is independent of r for $\lambda \gg r$ and $\nu \ll$ lowest resonant frequency (e.g., Hildebrand 1983). With these expressions one can compute the polarization spectrum, $P_{\text{mix}}(\lambda)$, for a mixture with any assumed set of values for the parameters.

From the relationship $dP/d\lambda \approx 0$ for individual grain species one is thus led to the following rule: a significant rise or fall in the polarization spectrum (for $\tau \ll 1$) will occur if and only if there is emission from two or more populations of grains with contrasting polarization properties *and* contrasting emission spectra. The emission spectra will differ if the populations differ in the wavelength dependence of (Q/r) or, below the Rayleigh-Jeans portion of the emission spectrum, if there are differences in temperature (Hildebrand et al. 1999).

Consider first a mixture of (discrete) graphite and silicate grains in a tenuous cloud where all grains are exposed to the interstellar radiation field. Assume temperatures (graphite ~ 20 K; silicate ~ 15 K) and relative abundances (graphite $\frac{1}{4}$ by volume) as proposed by Draine & Lee (1984) and dielectric functions as given by Draine (1985). The assumed dielectric functions result in nearly identical spectral indexes for the two grain species at $\lambda > \sim 50 \mu\text{m}$. The temperature differences are due to differences in the UV and optical absorptivities. From spectropolarimetry in the mid-infrared (Aitken 1996; Aitken et al. 1985, 1988) we know that silicate grains can be aligned. If we assume that graphite grains are not aligned (perhaps because they are too small or have low paramagnetic susceptibility), then the fraction of the emission from aligned grains will increase with wavelength and the polarization spectrum should have the form shown in Figure 16.

Finkbeiner et al. (1999) have fitted the submillimeter and microwave flux data of tenuous clouds with a two-

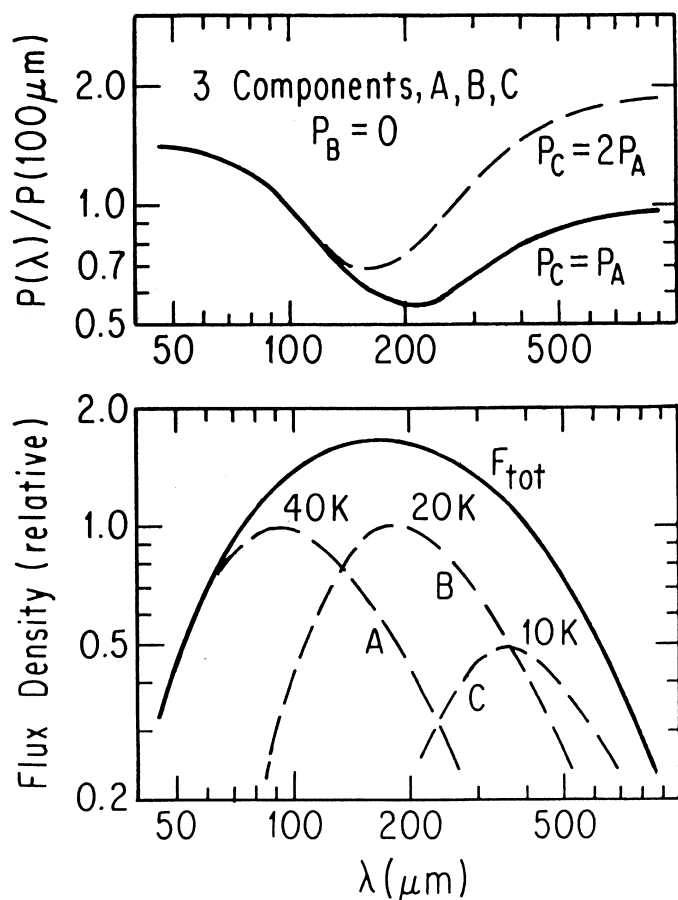


FIG. 18.—Polarization and flux spectra for a cloud with components at temperatures $T_A = 40$ K, $T_B = 20$ K, $T_C = 10$ K where only the components A and C are polarized. The solid polarization curve (upper panel) is drawn for relative polarization efficiencies, $P_C = P_A$, $P_B = 0$. The dashed curve is drawn for $P_C = 2P_A$, $P_B = 0$. The flux density curves (lower panel) are for peak flux densities in the ratio $1:1:\frac{1}{2}$. The flux spectra for the individual components have the form $\nu B(\nu, T)$.

component dust model consisting of cold (9.4 K) silicate grains with spectral index 1.67 and warmer (16.2 K) “graphite” grains with spectral index 2.7 (not in accord with Draine’s dielectric functions). As in the case of the model of Draine & Lee (1984), the fraction of the observed flux from the (aligned) silicate grains would increase with wavelength; again assuming zero (or low) polarization efficiency for graphite grains, one would expect a rising spectrum similar to that shown in Figure 16 but displaced toward longer wavelengths.

The temperatures of irradiated grains are influenced not only by the absorptivities of the grain materials but also by the cross sections of the grains with respect to anisotropic radiation fields (Onaka 2000). The observed polarization is influenced by the alignment of the grains with respect to the radiation source and the observer. This effect is likely to be significant near bright stars in cloud cores and may also play a role in the vicinity of low-luminosity embedded stars.

Next, consider a two-component model with temperature differences corresponding to two types of local environments; not to differences in grain properties (hence $[Q_i(\nu)/r_i]/[Q_j(\nu)/r_j] \equiv 1$). If hot grains near embedded stars are aligned and warm grains shielded from the embedded stars are not aligned, then the flux spectrum and polarization spectrum for the assumed temperatures should appear as shown in Figure 17.

As a final example, consider a cloud where, again, all grains are identical but where grains in three different environments are at different temperatures and are differently aligned. For example, hot aligned grains near embedded stars (component A); warm unaligned grains shielded from radiation (component B); and cold aligned grains on a surface layer removed from internal sources of heating and turbulence but exposed to radiation from the interstellar radiation field or nearby H II regions (component C). The grains in component B (shielded) are near equilibrium with the local environment. Those in A and C are far from equilibrium and thus satisfy a condition for alignment established by Lazarian et al. (1997). For such a cloud model the polarization and flux density spectra would have the forms shown in Figure 18 for the temperatures, relative peak flux densities, and relative polarization efficiencies indicated in the figure.

The results shown in Figure 15 indicate that the polarization spectrum does, indeed, fall and then rise again as in this three-component model. But before taking seriously this any other model for a given type of object, one should determine whether *both* the polarization spectrum *and* the flux density spectrum agree with the model over a wide range of wavelengths and at many points. Such determinations have yet to be done with the required accuracy.

The models illustrated here have been based on the approximation $dP/d\lambda \approx 0$ for individual grain species (expression [26]). Whether or not real grains obey that approximation, interpretations of far-infrared polarimetry must take into account variations in temperature and polarization efficiency (eqs. [27]–[29b]). When models have been tested point by point against flux and polarization spectra over broad spectral and spatial regions, it should be possible not only to infer large-scale magnetic structures but also to infer characteristics of domains within the clouds.

We thank J. Greaves, D. A. Harper, and J. Valée for comments on a draft of the paper, and we thank the referee, A. Goodman, for additional comments. This work was supported by NSF grant AST 97-32326. J. Dotson was supported by NASA/Ames Research Center Research Interchange grant NCC2-1134. G. Novak was supported by an NSF Faculty Early Career Development Award, OPP-9618319. J. Vaillancourt was supported by NASA Graduate Student Researcher Program grant NGT-563.

REFERENCES

- Aitken, D. K. 1996, in ASP Conf. Ser. 97, *Polarimetry of the Interstellar Medium*, ed. W. G. Roberge & D. C. B. Whittet (San Francisco: ASP), 225
- Aitken, D. K., Baily, J. A., Roche, P. F., & Hough, J. M. 1985, *MNRAS*, 215, 815
- Aitken, D. K., Roche, P. F., Smith, C. H., James, S. D., & Hough, J. M. 1988, *MNRAS*, 230, 629
- Aitken, D. K., Smith, C. H., Toby, Moore, T. J. T., Roche, P. F., Fujiyoshi, T., & Wright, C. M. 1997, *MNRAS*, 286, 85
- Arce, H. G., Goodman, A. A., Bastien, P., Manset, N., & Sumner, M. 1998, *ApJ*, 499, L93
- Baily, J., Chrystomou, A., Hough, J. H., Gledhill, T. M., McCall, A., Clark, S., Ménard, F., & Tamaura, M. 1998, *Science*, 281, 672
- Barvainis, R., Clemens, D. P., & Leach, R. 1988, *AJ*, 95, 510
- Bevington, P. R., & Robinson, D. K. 1992, *Data Reduction and Error Analysis for the Physical Sciences* (St Louis: McGraw-Hill)
- Bower, G. C., & Backer, D. C. 1998, *ApJ*, 496, L97
- Brogan, C. L., Troland, T. H., Roberts, D. A., & Crutcher, R. M. 1999, *ApJ*, 515, 304
- Chandrasekhar, S., & Fermi, E. 1953, *ApJ*, 118, 113
- Craig, I. J. D., & Brown, J. C. 1986, *Inverse Problems in Astronomy* (Bristol and Boston: Adam Hilger Ltd.)
- Cudlip, W., Furniss, I., King, K. J., & Jennings, R. E. 1982, *MNRAS*, 200, 1169
- Davidson, J. A. 1996, in ASP Conf. Ser. 97, *Polarimetry of the Interstellar Medium*, ed. W. G. Roberge & D. C. B. Whittet (San Francisco: ASP), 504
- Davis, C. J., Chrysostomou, A., Matthews, H. E., Jenness, T., & Ray, T. P. 2000, *ApJ*, 530, L115
- Dotson, J. L. 1996, *ApJ*, 470, 566
- Dotson, J. L., Dowell, C. D., Schleuning, D. A., & Hildebrand, R. H. 2000, *ApJ*, in press
- Dowell, C. D. 1997, *ApJ*, 487, 237
- Dowell, C. D., Hildebrand, R. H., Schleuning, D. A., Dotson, J. L., Davidson, J. A., & Houde, M. 2001, in preparation
- Dowell, C. D., Hildebrand, R. H., Schleuning, D. A., Dotson, J. L., Novak, G., Renbarger, T., & Houde, M. 1998, *ApJ*, 504, 588
- Dragovan, M. 1986, *ApJ*, 308, 270
- Draine, B. T. 1985, *ApJS*, 57, 587
- Draine, B. T., & Lazarian, A. 1998, *ApJ*, 508, 157
- Draine, B. T., & Lee, M. L. 1984, *ApJ*, 285, 89
- Draine, B. T., & Weingartner, J. C. 1996, *ApJ*, 470, 551
- Duncan, W. D., Robson, I., Ade, P. A. R., & Church, S. E. 1995, in ASP Conf. Ser. 75, *Multifield Systems for Radio Telescopes*, ed. D. T. Emerson & J. M. Payne (San Francisco: ASP), 295
- Emerson, D. T., Klein, U., & Haslam, C. G. T. 1979, *A&A*, 76, 92
- Finkbeiner, D. P., Davis, M., & Schlegel, D. J. 1999, *ApJ*, 524, 867
- Flett, A. M., & Murray, A. G. 1991, *MNRAS*, 249, 4P
- Haslam, C. G. T. 1974, *A&AS*, 15, 333
- Hildebrand, R. H. 1983, *QJRAS*, 24, 267
- . 1988, *QJRAS*, 29, 327
- . 1996, in ASP Conf. Ser. 97, *Polarimetry of the Interstellar Medium*, ed. W. G. Roberge & D. C. B. Whittet (San Francisco: ASP), 254
- Hildebrand, R. H., Dotson, J. L., Dowell, C. D., Schleuning, D. A., & Vaillancourt, J. E. 1999, *ApJ*, 516, 834
- Hildebrand, R. H., & Dragovan, M. 1995, *ApJ*, 450, 663
- Hildebrand, R. H., Dragovan, M., & Novak, G. 1984, *ApJ*, 284, L51
- Holland, W. S., et al. 1999, *MNRAS*, 303, 659
- Jeffrey, W., & Rosner, R. 1986, *ApJ*, 310, 463
- Jenness, T., Lightfoot, J. F., & Holland, W. S. 1998, *Proc. SPIE*, 3357, 548
- Jones, T. J. 1989, *ApJ*, 346, 728
- Jones, T. J., Klebe, D., & Dickey, J. M. 1992, *ApJ*, 389, 602
- Lazarian, A. 1997, *ApJ*, 483, 296
- Lazarian, A., Goodman, A. A., & Myers, P. C. 1997, *ApJ*, 490, 273
- Leach, R. W., Clemens, D. P., Kane, B. D., & Barvainis, R. 1991, *ApJ*, 370, 257
- Leahy, P., & Fernini, I. 1989, *VLA Scientific Memo.*, 161, 1
- Li, D., Goldsmith, P. F., & Xie, T. 1999, *ApJ*, 522, 897
- Lis, D. C., Serabyn, E., Keene, J., Dowell, C. D., Benford, D. J., Phillips, T. G., Hunter, T. R., & Wang, N. 1998, *ApJ*, 509, 299
- Martin, P. G., & Angel, J. R. P. 1976, *ApJ*, 207, 126
- Mather, J. C. 1982, *Appl. Opt.*, 21, 1125
- Matthews, B. C., & Wilson, C. D. 2000, *ApJ*, 531, 868
- Morris, M., Davidson, J. A., & Wernar, M. W. 1995, in *Proc. Airborne Astronomy Symp. on the Galactic Ecosystem: From Gas to Stars to Dust*, ed. M. R. Haas, J. A. Davidson, & E. F. Erickson (San Francisco: ASP), 477
- Myers, P. C., & Goodman, A. A. 1988, *ApJ*, 329, 392
- . 1991, *ApJ*, 373, 509
- Novak, G., Dotson, J. L., Dowell, C. D., Goldsmith, P. F., Hildebrand, R. H., Platt, S. R., & Schleuning, D. A. 1997, *ApJ*, 487, 320
- Onaka, T. 2000, *ApJ*, 533, 298
- Platt, S. R., Hildebrand, R. H., Pernic, R., Davidson, J. A., & Novak, G. 1991, *PASP*, 103, 1193
- Purcell, E. M. 1979, *ApJ*, 231, 404
- Rao, R., Crutcher, R. M., Plambeck, R. L., & Wright, M. C. H. 1998, *ApJ*, 502, L75
- Rice, S. O. 1947, *Bell System Tech. J.*, 27, 109
- Roberge, W. G., Hanany, S., & Messinger, D. W. 1995, *ApJ*, 453, 238
- Sault, R. J., & Macquart, J. P. 1999, *ApJ*, 526, L85
- Schleuning, D. A. 1998, *ApJ*, 493, 811
- Schleuning, D. A., Dowell, C. D., Hildebrand, R. H., & Platt, S. R. 1997, *PASP*, 109, 307
- Schleuning, D. A., Vaillancourt, J. E., Hildebrand, R. H., Novak, G., Dotson, J. L., Davidson, J. A., & Dowell, C. D. 2000, *ApJ*, 535, 913
- Serkowski, K. 1958, *Acta Astron.*, 8, 135
- Sievers, A. W., Mezger, P. G., Gordon, M. A., Kreyza, E., Haslam, C. G. T., & Lemke, R. 1991, *A&A*, 251, 231
- Simmons, J. F. L., & Stewart, B. G. 1985, *A&A*, 142, 100
- Stokes, G. G. 1901, in *Mathematical and Physical Papers of Sir George Stokes*, vol. 3 (Cambridge: Cambridge Univ. Press), 233
- Tamura, M., Hough, J. H., Greaves, J. S., Morino, J.-I., Chrisostomu, A., Holland, W. S., & Munetake, M. 1999, *ApJ*, 525, 832
- Wardle, J. F. C., & Kronberg, P. P. 1974, *ApJ*, 194, 249
- Vallée, J. P., & Bastien, P. 2000, *ApJ*, 530, 806
- van de Hulst, H. C. 1957, *Light Scattering by Small Particles* (New York: Dover)
- Zweibel, E. G. 1996, in ASP Conf. Ser. 97, *Polarimetry of the Interstellar Medium*, ed. W. G. Roberge & D. C. B. Whittet (San Francisco: ASP), 486